Raman spectroscopy to determine CO2 solubility in mafic silicate melts at high pressure: Haplobasaltic, haploandesitic and approach of basaltic compositions

Julien Amalberti, Philippe Sarda, Charles Le Losq, Nicolas Sator, Tahar Hammouda, Eva Chamorro-Pérez, Bertrand Guillot, Sylvie Le Floch, Daniel Neuville

Raman spectroscopy to determine CO_2 solubility in mafic silicate melts at high pressure: haplobasaltic, haploandesitic and approach of basaltic compositions

Julien Amalberti[1,2], Philippe Sarda[1,3,4]*, Charles Le Losq[2], Nicolas Sator[5,6], Tahar Hammouda[7,8,9], Eva Chamorro-Perez[3,4], Bertrand Guillot[5,6], Sylvie Le Floch[10] and Daniel R. Neuville[2]

[1] Université Paris-Saclay, CNRS-GEOPS, Rue du Belvédère, Bât. 504, 91405 Orsay, France

[2] CNRS-IPGP, Université de Paris, 1 rue Jussieu, Paris F-75005, France

[3] ENS de Lyon, Laboratoire de Géologie de Lyon, UMR 5276, 15 parvis René Descartes, F-69342 Lyon Cedex 07, France

[4] CNRS, F-69342 Lyon Cedex 07, France

[5] Sorbonne Universités, UPMC Univ. Paris 6, UMR 7600, LPTMC, Paris F-75005, France

[6] CNRS, Paris F-75005, France

[7] Université Blaise Pascal Clermont-Ferrand 2, Laboratoire Magmas et Volcans, UMR-CNRS 6524, UMR-IRD 163, Clermont-Ferrand F-63038, France

[8] CNRS, Clermont-Ferrand F-63038, France

[9] IRD, Clermont-Ferrand F-63038, France

[10] Institut Lumière Matière, Université Lyon1 – CNRS, UMR 5306, Université de Lyon, 69622 Villeurbanne, France

* corresponding author: philippe.sarda@universite-paris-saclay.fr

Keywords: Carbon dioxide; basaltic melt; andesitic melt; solubility; high pressure; confocal micro-Raman spectroscopy; molecular dynamics simulation

Abstract:

CO_2 degassing of mafic silicate melts is an important part of the terrestrial carbon cycle, at mid-ocean ridges, oceanic hot spots, or in the middle of continents. Deeper CO_2-bearing mafic magmas may also exist, such as those suspected in the D'' zone, and certainly existed in the magma ocean of the early Earth. Knowledge of the CO_2 solubility in mafic melts at high pressure is therefore important but unknown at present. Results from molecular dynamics simulation (e.g., Guillot and Sator, 2011) predict that CO_2 solubility in basalt may be much higher than previously thought at pressures and temperatures relevant to the upper mantle. But some recent models predict low solubility at high pressure (e.g., Eguchi and Dasgupta, 2018). The present study thus experimentally investigates the solubility of CO_2 in basalt and andesite in the pressure range 1.5-8.5 GPa at 1820-2130 K in oxidizing conditions. Up to 4 GPa, the quenched samples are essentially vitreous and CO_2-saturated. Their CO_2 contents are measured using confocal micro-Raman spectroscopy, where we establish an internal calibration line relating CO_2 content to the area of the Raman band assigned to the ν_1 stretching vibration of carbonate groups. This calibration appears independent from the spectrometer, sample or experimentalist, thus enhancing confidence in this method. At 5 and 8.5 GPa, the quenched samples are found partially crystallized. Their CO_2 abundance is estimated at micro-scale from Raman mapping, and at large scale from image

analysis and presence/absence of vesicles. Over the 1.5-8.5 GPa pressure range, obtained CO_2 concentrations vary between 1.8 and >13.6 wt.%. At 5 GPa and 1873 K, the CO_2 content in basalt and andesite are similar. These findings experimentally confirm the ability of mafic melts to accommodate large amounts of CO_2 at conditions prevailing in the deep Earth. A consequence is that magmas issued from partial melting of carbonate-bearing silicate rocks may ascend with significant quantities of CO_2 of several wt.% and more: when reaching shallower depths, they may degas large quantities of CO_2. Present estimates of the global carbon flux to the atmosphere may thus be underestimated, and implications to early magma ocean degassing may be considered. Other consequences may concern the genesis of kimberlites and carbonatites. We finally speculate that, if silicate melts exist in the D" zone, significant amounts of carbon may be stored there, and consequences may arise as to carbon sequestration in the core.

1. Introduction

CO_2 and H_2O are the two most abundant volatile species of the inner planets (Gerlach and Nordlie, 1975). On the Earth, they constitute a great deal of several external reservoirs such as the atmosphere, the oceans or the carbonates of the crust, and play a fundamental role in determining past and present surface temperatures (Ringwood, 1966; Cameron, 1973). They are also important in geodynamics because of their effects on the mantle solidus and liquidus as well as on the properties of melts (Kushiro et al., 1968; Eggler, 1976; Kawamoto and Holloway, 1997; Dasgupta and Hirschmann, 2006; Green et al. 2010; Pommier et al. 2012, Hammouda and Keshav, 2015). Therefore, it is important to understand their behavior in planetary processes.

In this paper, we focus on CO_2. Since basalt is the main magma type resulting from melting of the terrestrial interior, and probably other planetary interiors (Stanley et al., 2012), we study the question of how much CO_2 can be dissolved in basaltic melts (and one intermediate).

At present, basaltic melts are produced mainly at mid-ocean ridges, subduction zones and hot spots, but it has been suggested that melt could also be present close to the core, in the so-called D'' zone between about 2800 and 2900 km depth (Labrosse et al., 2007).

Solubility of CO_2 in melt controls degassing, i.e., the way CO_2 exits the solid Earth, an important part of the carbon cycle, past and present (Dasgupta and Hirschmann, 2010). In very ancient geological times, degassing occurred massively as recorded by noble gas isotopes (e.g., Sarda et al., 1985), probably in the shallow regions of a magma ocean (e.g., Elkins-Tanton, 2012). Such degassing mainly released H_2O and CO_2 since this magma ocean was likely H_2O- and CO_2-rich (e.g., Marty, 2012), contributing to establish the P,T conditions at the surface, which in turn influenced magma ocean cooling (e.g. Lebrun et al., 2013; Hamano et al., 2013).

In these ancient times, the silicate Earth may have been completely molten (e.g., review in Elkins-Tanton, 2012), hence the terrestrial magma ocean was possibly as deep as the present core–mantle boundary (CMB). Work on heat in the Earth raised the hypothesis that the magma ocean did not crystallize at great depth, thus generating the so-called basal magma ocean (Labrosse , 2007; Coltice et al., 2011). That melt may have existed at such great depths raises the question of how much carbon it could have contained, an important question for carbon partitioning with iron (e.g., Chi et al., 2014), given that carbon could be among the light elements in the

present core (e.g., Wood, 1993). These matters are currently the subject of experiments and discussions (e.g., Grewal et al., 2019), but knowledge of CO_2 solubility in melt at such very high pressure is necessary to better understand carbon sequestration into the core during its early differentiation.

At present, and for more recent geologic times, high pressure CO_2 solubility in melt is important everywhere deep magmas may exist. One example is given by the low velocity seismic anomalies evidenced in the D'' zone (e.g., Vinnik et al., 1998), just above the CMB, which may be explained by the existence of silicate melts (e.g., Williams and Garnero, 1996; Coltice et al., 2011).

Other examples include the above-mentioned degassing of basaltic melts ascending at Mid-Oceanic Ridges or subduction zones, witnessed by numerous CO_2 vesicles in samples (e.g. Moore, 1978; Sarda and Graham, 1990; Chavrit et al., 2014), continental magmatism, where degassed CO_2 may be stored in sedimentary basins (e.g., Ballentine et al. 1991; Ballentine, 1997), the rare occurrence of carbonatites in continental areas (Woolley and Church, 2005) and some oceanic islands (Mourão et al., 2012), or else the existence of kimberlites (Sparks et al., 2006; Mitchell, 2008), which are derived from carbon-rich silicate melts (Brooker et al., 2011).

Concerning depth and pressure, the latter examples probably involve CO_2 melts in the first 100-300 km of the Earth, i.e., pressures up to roughly 10 GPa, and studies of the magma ocean degassing or of the D'' zone require knowledge of CO_2 solubility at much higher pressures, up to ~100 GPa.

Solubility of CO_2 in silicate melts has been both documented in an experimental way and approached in a theoretical way. On the experimental side, early studies reach relatively low pressures and used silicic compositions because experiments are easier (see reviews in Blank and Brooker, 1994; Ni and Kepler, 2013). More recently, higher pressures were reached but, for mafic compositions, few studies achieve pressures higher than 1 GPa, and very few higher than 3 GPa (review in Iacono-Marzano et al., 2012). On the theoretical side, often to interpret experimental data, a first approach developed classical models based on macroscopic thermodynamics yielding a very abundant literature (e.g., Khitarov et Kadik, 1973; Dixon et al., 1995; Papale, 1999; Behrens et al. 2004; Iacono-Marzano et al., 2012). These models are essentially empirical and include parameters that are adjusted to reproduce experimental data.

Another theoretical approach is molecular dynamics (MD), where the very atoms are simulated in their relations with all the other atoms of their environment, allowing their interactions and their bonds to be reproduced from basic principles (e.g., Genge et al., 1995 for carbonate melt). Although ab initio calculation is in principle possible, it is practically difficult to be used for the complex silicate melts, demanding short simulation times and small numbers of atoms, but being possible in the case of crystals (e.g., Gerin et al., 2017). Whereas pioneering studies of silicate melts by ab initio calculations exist (Vuilleumier et al., 2015), current simulations are based on a force field determined previously (Guillot and Sator, 2007a,b), and constantly refined (e.g., Dufils et al., 2017).

A molecular dynamics simulation study (Guillot and Sator, 2011) has shown that the CO_2 amount a silicate melt can dissolve at high pressure far exceeds the amount predicted by the Henry's law constrained by low-pressure data, e.g., ~20 wt.% CO_2 in MORB at 8 GPa and 1873K, as compared to ~4 wt.%. The simulation of Guillot and Sator (2011) also confirms that the high-pressure CO_2 solubility increases with increasing number of non-bridging oxygen atoms (NBOs) in

the melt (e.g., Verweij et al., 1977; Brooker et al., 2001a). Though these simulation results agree with the few solubility data for mafic compositions available at moderate pressures of 1-2 GPa (Mattey, 1991; Pan et al., 1991; Stanley et al., 2012; Li et al., 2017) and more recently up to 3 GPa (Stanley et al., 2011; Eguchi and Dasgupta, 2017), experimental data at pressure above ~3 GPa is still lacking. Moreover, the recent model of Eguchi and Dasgupta (2018) contradicts the simulation of Guillot and Sator (2011) in predicting low CO_2 concentrations at pressures above ~5 GPa. Only one recent study exists for pressures higher than 3 GPa, that of Kim et al. (2018) at 6 GPa, where 15 wt.% CO_2 was measured using Nuclear Magnetic Resonance (NMR) spectroscopy, and it agrees with the very high CO_2 solubilities suggested by the simulations, although it is for an albitic composition.

To extend the pressure range where the solubility of CO_2 in basaltic melts is known, we performed high pressure - high temperature experiments on CO_2-bearing mafic and intermediate samples in the pressure range 1.5-8.5 GPa, at about 1820 - 2130 K, and in oxidizing conditions. This is a challenging task because very high temperatures must be reached and maintained at high pressure. Of course, the melts used here are not natural melts, but are as close as possible, with the techniques used. We are aware that our results only approach the behavior of natural melts, but we are confident that they must be quite close as indicated by comparison with previous experimental results or with theoretical simulations (section 4).

At pressures higher than ~1 GPa, the amount of dissolved CO_2 is larger than 1 wt.%. At such concentrations, Fourier transform infrared (FTIR) spectroscopy, which is routinely used to measure CO_2 solubility (e.g., Stolper and Holloway, 1988; Dixon et al. 1995; Eguchi and Dasgupta, 2017), becomes difficult to use because most of the IR photons are absorbed by the sample, which demands samples to be vanishingly thin (see Brooker et al., 1999).

The alternative we use here is Raman spectroscopy. Indeed, Raman spectroscopy has demonstrated its efficiency to quantify various volatiles in silicate glass, such as H_2O (Thomas, 2000; Chabiron et al., 2004; Behrens et al., 2006; Mercier et al., 2010; Le Losq et al. 2012), SO_4^{2-} (Manara et al., 2007; Lenoir et al., 2009, 2010) or N_2 (Roskosz et al., 2006). About CO_2, Raman spectroscopy was recently used to measure the density of CO_2 in bubbles present in melt inclusions of minerals, and, coupled with optically measured vesicularity, to yield the CO_2 concentration in the inclusion (Capriolo et al. 2020). For direct measurement of CO_2 present in silicate melt or glass using Raman spectroscopy, feasibility studies appeared first (Sarda et al., 2009; Amalberti et al., 2011a,b) and Morizet et al. (2013) more recently published a calibration for this method.

In the present work, we thus use Raman spectroscopy to measure the CO_2 content of glasses synthetized at high pressure, that were saturated in CO_2 as indicated by the presence of a bubble. For partially crystallized samples synthesized at $P \geq 4$ GPa, analysis of microscope images or the absence of any vesicle allows estimating the fraction of dissolved CO_2. To discuss those experimental data, we also report results from a molecular dynamic simulation of CO_2-bearing silicate melts, using the force field of Guillot and Sator (2011).

2. Experimental set up

2.1. Starting materials and high-pressure experiments

In this study, we focus on mafic melts and tried to approach basaltic and andesitic compositions. Of course, the prepared samples approach basalt and andesite as close as possible, but, as explained below, it is impossible to experiment on compositions rigorously identical to basalt and andesite. In the following, we may use the terms basalt and andesite, keeping in mind that the reported experiments used starting compositions, given in Table 1, that differ to some extent.

Internal calibration of Raman analysis for CO_2

For this work, internal calibration is based on two kinds of samples. One is potassium silicate glass prepared at ambient pressure, for which dissolved CO_2 was previously quantified and published. We used two potassium silicate glass aliquots, dubbed KS here, obtained by Bourgue and Richet (2001). One of these is without CO_2. The other was prepared by melting a mixture of powdered SiO_2 and K_2CO_3. Dissolved CO_2 of the latter sample was quantified by these authors using a LECO® cell, giving a CO_2 concentration of 3.6 wt.% (Bourgue and Richet, 2001) More details are given in section 2.3.

The other kind of sample used for internal calibration is a selection of our studied samples, for which H_2O was also quantified by Raman spectroscopy following the method of Le Losq et al. (2012), and the CO_2 was then deduced from the budget of all the major elements plus water (Table 2 and section 2.3).

Basaltic natural and synthetic samples exposed to pressures up to 5 GPa with a Belt-type press

For high temperature - high pressure (HT-HP) experiments with pressure in the range 1.5–4 GPa, a CO_2-bearing starting material close to the basaltic composition was prepared by mixing a tholeiite glass from the South Atlantic Ocean labeled EW9309 14D-4g (Douglass et al., 1999) with an amount of powdered calcite, large enough for the resulting basaltic melt to be CO_2-saturated at such pressures (> 10 wt.% CO_2). The corresponding samples are named BPhE2 and BPhE3 in Tables 1 and 2.

For comparison, and to avoid iron loss to the platinum capsule (e.g., Gudmundsson and Holloway, 1993), an iron-free starting material was prepared by mixing appropriate amounts of high purity powdered oxides (SiO_2, TiO_2, Al_2O_3 and MgO) and carbonates ($CaCO_3$ and Na_2CO_3), the composition of the resulting HT-HP melt being haplo-tholeiitic (samples BPhE10, BPhE11 and BPhE12 in Tables 1 and 2). The resulting CO_2 concentration was calculated to be ~10.8 wt.% CO_2, large enough to saturate the silicate melt in CO_2 at pressures of 1.5-4 GPa. Of course, iron has important influence on physical properties of melts (e.g., Chevrel et al., 2013 about rheology), but our results on these compositions are only a tentative approach of reality. However, we recall that Fe^{2+}, in contrast to K^+, Na^+ and Ca^{2+}, is a cation that has the weakest influence on CO_2 solubility together with Mg (Brooker et al., 2001a).

All the above samples were placed into a platinum capsule that was arc-electrically welded. They were exposed to high pressures using a Belt-type press at Institut Lumière Matière, Université Claude Bernard Lyon1, France (e.g., Toulemonde et al., 2005). The cell assembly includes a pyrophyllite sleeve, with two pyrophyllite gaskets and two steel plugs (see Fig.2 in San Miguel and Toulemonde, 2005), that receives the sample assembly composed of a graphite furnace, a periclase sleeve and the sample capsule. Pressure is not measured but known from

laboratory calibration with an estimated 1σ error of 5% (Table 2). Melting basaltic compositions under such high pressures requires very high temperatures of 1500°C-1800°C, depending on pressure, which are difficult to obtain. An assembly minimizing heat loss, including a graphite furnace and a periclase sleeve receiving the platinum capsule, was thus especially designed, and realized for these experiments (Supplement, Fig. S1).

With this press, the assembly rapidly creeps at high pressure when exposed to such high temperatures. Therefore, experiments did not last more than 30 min. Heating was interrupted by turning off electrical power, which is expected to chill melt into glass with minimum crystallization. The observed cooling rate is ~2 degrees/s, a relatively slow value compared to the multi-anvil press also used in this study (see below), probably due to the pyrophyllite sleeve acting as a thermal insulator (also reported in Liu et al., 2015). Pressure was then slowly brought back to ambient, to avoid cracks as far as possible.

The assembly has no routine thermocouple, and, because of creeping, it is impossible to calibrate temperature up to the values reached in our experiments. Because temperature should have a weak influence on CO_2 solubility, our intention was to obtain complete melting, even if temperature was not accurately known. We thus initially used temperature estimates available in the laboratory from applied electrical power. Later, we performed careful experiments dedicated to temperature calibration using S-type Pt10%Rh-Pt thermocouples up to ~1000°C and extrapolated to the highest power values. The temperatures obtained for BPhE samples have an estimated 1σ error of ~50°C and are reported in Table 2. They are higher than initially assumed by up to 200 degrees. Therefore, the platinum capsules were probably very soft. Indeed, we observed that, in most of the BPhE experiments, a cavity is present within the Pt metal at the top of the capsule, certainly the remnant of a CO_2 bubble (e.g., Fig. S2A for BPHE11). Although known with some uncertainty, such high temperatures give supplementary assurance that the starting material indeed melted completely, and these cavities suggest that melts were indeed CO_2-saturated.

Basaltic and andesitic synthetic samples up to 8.5 GPa with a multi-anvil press

Another series of experiments were carried out using a multi-anvil press at pressures from 5 to 8.5 GPa. Two other glasses were synthesized from reagent grade powders of MgO, Al_2O_3 and SiO_2 mixed in the right proportions to obtain, after melting at 1923 K, a first glass with 63 mol.% SiO_2, 18 mol.% Al_2O_3, and 19 mol.% MgO, and a second glass with 76 mol.% SiO_2, 17 mol.% Al_2O_3, and 7 mol.% MgO. To ensure getting glass with no vestige of any crystal, the initial mixture was melted in air at 1350°C for 12 hours and up to 1650°C for 2 additional hours, then quenched, grinded, and melted again, such a cycle been repeated no less than 4 times (Neuville et al., 2008).

To these compositions was added a carbonate mixture of reagent grade powders of $MgCO_3$, $CaCO_3$ and Na_2CO_3 to obtain, respectively, a basaltic glass powder (samples 1010 and 1011), and an andesitic glass powder (sample 1090), both with excess CO_2. This CO_2 excess was calculated to be ~13.6 wt.% for samples 1010 and 1011, and ~9.0 wt.% for sample 1090 (see Table 1).

The multi-anvil press allowed us to achieve higher pressures than the Belt press. These experiments were performed at the "Laboratoire Magmas et Volcans" in Clermont-Ferrand (France). A Pt capsule contains the sample and is closed by electric arc welding. This Pt capsule is placed into a cell assembly that includes a ceramic octahedron, a ZrO_2 sleeve used as thermal

insulator, a $LaCrO_3$ furnace, and an MgO sleeve around the Pt capsule (Hammouda, 2003). This cell assembly is then placed into a multi-anvil press (Kawai and Endo, 1970) with a Walker-type module (Walker et al., 1990). Pressure is not measured but known from laboratory calibration with a 1 σ error of 0.25 GPa (Table 2). During each experiment, temperature was monitored by a W-Re thermocouple routinely placed above the Pt capsule and was regulated at 1873±1 K (1σ). Temperature gradient across the assembly is estimated to ±50°C so that the 1 σ uncertainty on sample temperature is estimated to be 25°C (Table 2). Experiments ran for several hours, making it safer that equilibrium was reached. After having been exposed to HT-HP conditions, the melt was quenched by turning off electrical power, where the cooling rate is on the order of 100 K/s (Hammouda, 2003).

Redox state estimate

We did not attempt to measure the redox state in our samples. For all the experiments, samples were contained in a platinum capsule. No reduced material was at the contact with capsules during runs: in BPhE experiments, the carbon furnace was always outside the platinum capsule, separated from it by the periclase sleeve, and, in experiments run with the multi-anvil press, the capsule was located in a MgO sleeve, while the furnace around it is made of $LaCrO_3$, both being surrounded by a ZrO sleeve and a MgO octahedron, all these being oxidized compounds.

No attempt was done to vary the redox state in the present experiments. Hence, we believe our samples remained in a relatively oxidizing state, i.e., close to that of a natural basalt from Mid-Ocean Ridges with an oxygen fugacity of $\sim FMQ - 0.4$ (e.g., Bézos and Humler, 2005; FMQ is the fayalite-magnetite-quartz buffer).

This conclusion is supported by the Raman spectra of our iron-bearing samples, where the raw spectra leave no doubt as to the presence of iron as Fe^{3+} in the melt (see below, section 2.3.; e.g., Magnien et al., 2006, 2008; Roskosz et al., 2008; Cochain et al., 2012; Le Losq et al., 2019). Our measured CO_2 concentrations do not contradict this conclusion, since, according to Li et al. (2017), our *lowest* value (~1.6 wt.%) points to $\log fO_2$ being above ~IW + 2.5 (roughly 1.3 logs units below the MORB value of Bézos and Humler, 2005).

Measurements on samples brought back to ambient pressure

The CO_2 contents in the samples back from HP-HT were determined by Raman spectroscopy, since FTIR is difficult to use at such high CO_2 concentrations (Table 2). The chemical composition of the run products (Table 2) was obtained from electron microprobe analyzes performed at Clermont-Ferrand for BPhE samples, and at University Pierre et Marie Curie, in Paris, for samples 1010, 1011 and 1090.

2.2. Raman spectroscopy analyzes

Raman spectrometry

Raman spectra were recorded using a triple grating T64000 Jobin-Yvon® Raman spectrometer equipped with a confocal system, a 1024 charge-coupled device (CCD) detector cooled by liquid nitrogen and an Olympus® microscope. The optimal spatial resolution is 1-2 μm^2 with an x100

296 Olympus® objective, and the spectral resolution is 0.7 cm^{-1}. A Coherent® laser 70-C5 Ar^{+}, having a
297 wavelength of 514.532 nm, is used as the excitation line, with a laser power of 150 to 250 mW. No
298 damage caused by the laser was observed, even for high iron content samples (Magnien et al.,
299 2006). All spectra were acquired in the 15-4000 cm^{-1} frequency-range, with an exposure time of
300 300 s in 3 repetitions. For an optimum signal/noise ratio, the Raman spot was focalized at 10 µm
301 below sample surface (Behrens et al., 2006). Raw Raman spectra are given in supplement Fig. S3.
302
303 *Preliminary treatment of Raman spectra*
304 After acquisition, all spectra were corrected for temperature and excitation line effects by
305 applying the Long correction (Shuker and Gammon, 1970; Long, 1977; Galeener and Sen, 1978;
306 Mysen et al., 1982). Then, background was subtracted following the protocol described in Le Losq
307 et al. (2012). The background is defined by a generalized cross-validation cubic spline baseline
308 (Craven and Wahba, 1979; Woltring, 1986) that is fitted to portions of Raman spectra devoid of
309 signal (Fig. 1a and Fig. S3). After baseline subtraction, spectra were normalized to their maximum
310 intensity, and these successive steps are illustrated in Fig. 1a. Then, as described next, a
311 deconvolution procedure was applied to the region of interest to extract the carbonate peak (Fig.
312 1b). For clarity, these four successive stages of treatment are also illustrated in Fig. S4 for one
313 spectrum.
314
315 **2.3. CO_2-related Raman peaks and calibration**
316
317 *Raman peaks and their deconvolution*
318 When CO_2 dissolves into a silicate melt, it is incorporated either under the molecular form (CO_2)
319 or as carbonate ion (CO_3^{2-}). By analogy between Raman and infrared spectra of fluid CO_2 and
320 carbonates, the Raman bands due to CO_2 and CO_3^{2-} present in silicate glasses have been known for
321 long (Verweij et al., 1977; Sharma, 1979; Mysen and Virgo, 1980; Rai et al., 1983; Brooker et al.,
322 1999; Bourgue and Richet, 2001): a weak band at ~ 650 cm^{-1} corresponds to a bending mode of
323 CO_3^{2-} (out of the molecule plane), a strong band at ~ 1080–1090 cm^{-1} is associated with the
324 symmetric stretching mode (v_1) of CO_3^{2-} and a doublet in the region of 1400-1500 cm^{-1} is due to
325 the asymmetric stretching vibrations (v_3) of CO_3^{2-} (Fig. 1a); molecular CO_2 generates a doublet in
326 the 1286-1388 cm^{-1} range (see Burke and Lustenhouwer, 1987). For comparison, the molecular
327 CO_2 doublet in gas hydrates is at 1274-1382 cm^{-1} (Nakano et al., 1998). In silicate glasses of
328 basaltic composition, it is believed that CO_2 is dissolved essentially under the form of carbonate
329 ions (Stolper and Holloway, 1988; Mattey, 1991; Pan et al., 1991; Dixon et al. 1995; Brooker et
330 al., 1999, 2001a,b) and, besides, we found no evidence for molecular CO_2 in any of the Raman
331 spectra of our quenched samples (e.g., Fig. 1a). Therefore, we use the intense peak assigned to
332 symmetric stretching vibrations of the carbonate ion at 1080-1090 cm^{-1} to quantify the global CO_2
333 content in the samples.
334 However, contrary to the peak assigned to O-H stretching in hydrous glasses that allows
335 quantification of water (Fig. 1a), the ~1085 cm^{-1} peak is mixed with signals from T-O (T=Si, Al)
336 stretching vibrations in Q^n units (i.e., SiO_4 and AlO_4 tetrahedra with *n* bridging oxygens (Schramm
337 et al., 1984). We thus need to separate the peak due to CO_3^{2-} symmetric stretching from the

signals generated by T-O stretching. To do so, corrected-normalized Raman spectra are fitted using a combination of Gaussian bands, as documented in Mysen et al. (1982) (see also Mysen, 1990; Neuville, 2006 and Le Losq et al., 2014). Fig. 1b shows examples of this deconvolution procedure (more examples are given in Fig. S5). The number of peaks depends on the glass chemical composition, i.e., on its initial depolymerization: obtained peaks at wavenumbers of 800, 880, 950, 1100 and 1150-1200 cm^{-1} are assigned to Si-O symmetric stretching in Q^0, Q^1, Q^2, Q^3 and Q^4 units respectively (Brawer and White, 1975, 1977; Virgo et al., 1980; Mysen et al., 1982; McMillan, 1984). One peak near 1050 cm^{-1} is also obtained, that can be assigned to asymmetric stretching of Si-O bonds in Q^n units (Le Losq et al., 2014 and references therein).

We remark that the peak at ~1000 cm^{-1} in Fig. 1b that is assigned to Q^3 is in fact a combination of Q^3 and Fe^{3+} (e.g. Magnien et al., 2006, 2008; Roskosz et al., 2008; Cochain et al., 2012; Le Losq et al., 2019) and this is seen on the subtle shoulder of the raw spectrum in this region. The occurrence of Fe^{3+} indicates the oxidized state of our samples (see discussion above).

Then, the area of all the peaks found are measured and that assigned to CO_3^{2-} is normalized to the sum of the areas of *all* the deconvoluted peaks, including CO_3^{2-} itself, as illustrated by relation (1):

$$A_{CO_3^{2-}} = \frac{a(CO_3^{2-})}{\sum_{i=0}^{4} a(Q^i) + a(CO_3^{2-})} \quad (1)$$

where $A_{CO_3^{2-}}$ is the carbonate normalized peak area, $a(CO_3^{2-})$ is the raw carbonate peak area, and $a(Q^0), a(Q^1), a(Q^2), a(Q^3), a(Q^4)$ are the raw areas of the silicate peaks. Obtained values of the $A_{CO_3^{2-}}$ normalized area are given in Table S1 for samples BPhE3, BPhE10, and 1010.

Calibration of CO_2 measurement (Fig. 2)

The peak area is proportional to the number of vibrators. We thus assume a linear relationship between the CO_3^{2-} normalized peak area and the concentration of dissolved CO_2, noted C_{CO_2},

$$A_{CO_3^{2-}} = a \times C_{CO_2}(wt.\%) \; . \quad (2)$$

For calibrating relation (2), we first have the two KS samples (section 2.1) for which the CO_2 concentration was determined by Bourgue and Richet (2001) to be zero (base melt $KS_{1.3}$ in (Bourgue and Richet, 2001)) and 3.6 wt.% (sample K2-1 in (Bourgue and Richet, 2001)). We remark that the CO_3^{2-} band in KS samples was found at 1046 cm^{-1}, not at 1080 cm^{-1}, certainly related to the particular chemical composition of these samples.

As other standard glasses, we use the basaltic samples BPhE2, BPhE3, BPhE10, BPhE12 and 1010, for which we used another part of the recorded Raman spectra to determine their water contents using the Raman-based method of Le Losq et al. (2012). These water values are given in Table 2 and are the average of several determinations across each sample. The water determinations for each spectrum of each sample are given in Table S1. Averaged over all the measurement spots, these H_2O values are between 0.5 and 2.6 wt.% (Table 2), and, adding them to the sum of the major element concentrations obtained by electron microprobe, the CO_2 content was determined by difference to 100% for each of the Raman spots. We then calculate, for each sample, the average of these CO_2 concentrations, and couple it to the average of the CO_3^{2-} normalized peak areas measured for the several spots. For sample 1010, this procedure was

performed on 12 spots, and compared to two additional spots, giving three reasonably well grouped points (Fig. 2).

We thus have 7 samples for calibration (Table 2): zero, KS, BPhE2, BPhE3, BPhE10, BPhE12 and 1010, with CO_2 values between zero and ~6 wt.% (9 points when using the three points of sample 1010). These points are reasonably aligned when plotting CO_2 concentration versus CO_3^{2-} normalized peak area, thus defining a calibration line for CO_2 measurement (Fig. 2). The slope of this line yields a value of 0.063453±0.002156 (1σ) for calibration coefficient a. This technique was presented in abstract form (Sarda et al., 2009; Amalberti et al., 2011a,b), and, at this time, we considered this calibration as preliminary because it included only three points.

Morizet et al. (2013) also reported on quantifying CO_2 in silicate glasses using Raman spectroscopy. They obtained a very similar (identical within error) calibration line with a value of 0.0659±0.0007 (1σ) for coefficient a (see eq.1). But those authors have 143 data points, as well as samples with various chemical compositions and up to 16 wt.% CO_2. We remark that Morizet et al. (2013), in describing their procedure, indicate they normalize the CO_3^{2-} peak area to the sum of the Q^n silicate peaks only. The almost identical calibration lines obtained here and by Morizet et al. (2013) suggest that Morizet et al. (2013) normalize in reality to the sum of the areas of all the deconvoluted peaks including the CO_3^{2-} peak, as we do here. We also remark that the calibration of Morizet et al. (2013) was slightly modified by Morizet et al. (2017).

The calibration line thus appears independent on the chemical composition of samples and independent on the Raman spectrometer (particularly its detector). The former is explained by the fact that the silicate and CO_2 peaks are affected in the same way by the changes in acquisition conditions that could be induced by variable chemical composition, so that their ratio is independent of them. The latter is explained by the fact that the silicate and CO_2 signals lie in the same frequency range, and hence, are affected in the same way by the specifications of the spectrometer. This is not the case for water measurement, because of the large frequency difference between the signals from silicate vibrations and O-H stretching (Fig. 1 and Le Losq et al., 2012). In addition, the strong similarity of these calibrations further suggest that results are also independent on the experimentalist.

We estimate the global uncertainty on normalized peak area determination to lie within 10 to 20%, depending on the sample. This is equivalent to 2-σ and thus, we use a conservative 1-σ value of 10% for all our peak area data, which we then propagate in a quadratic manner through equation (2): as the 1-σ error on our obtained calibration coefficient is of 3.3%, the 1-σ error on the obtained CO_2 concentration is dominated by the error on peak area, and it is on the order of 10%. In three cases, as discussed below, we made several measurements on the same sample to obtain a cartography of the CO_2 concentration: sample BPhE10 exhibits a large dispersion of the CO_3^{2-} concentration showing a distribution characterized by a 1-σ value of 51%, while other samples are much more homogeneous such as BPhE3, with a 1-σ of 5.9%, and sample 1010, with a 1-σ of 8.9%. Such a variable dispersion is a real feature, due to variable sample heterogeneity. Therefore, Raman measurement of CO_2 concentrations is quite accurate, in the sense that it yields a value close to the true one, and we estimate this accuracy to about 1%. On the other hand, there may be an up to 10% 1-σ uncertainty on the precision of the CO_2 concentration, expressing the

dispersion due to the measurement technique itself. Of course, these values do not take sample heterogeneity into account, which is a natural feature.

From an analytical point of view, Raman spectroscopy thus appears to be a useful way of measuring CO_2 in silicate glasses for relatively elevated CO_2 concentrations (e.g., Morizet et al., 2014; Morizet et al., 2020). The possibility of such a measurement relies on the detection and measurement of the carbonate peak that depends on the how well this peak can be separated from the bulge in the spectrum due to the Q^n and Fe^{3+} peaks. We empirically estimate a lower detection limit of 0.5 - 1 wt.% CO_2, depending on the silicate matter investigated. When possible, quantification of CO_2 is rapid, does not depend on acquisition conditions and glass composition, and as suggested by comparison with other laboratories, on the type of Raman spectrometer.

3. Results

3.1. CO_2 concentrations in vitreous samples

Silicate melt and CO_2 bubbles

CO_2 contents were determined by Raman spectroscopy (Table 2) for samples BPhE2 and BPhE3 (a MORB composition doped in CO_2, exposed to 2 and 3 GPa respectively and ~1920-2000 K), BPhE10, 11 and 12 (an iron-free haplobasalt composition doped in CO_2, exposed to 1.5, 2 and 4 GPa respectively and 1820-2130 K), and sample 1010 (an iron-free haplobasaltic glass doped in CO_2, exposed to 5 GPa and 1873 K).

A visual inspection of these samples shows the presence of cavities, either within the bulk silicate sample in contact with the Pt capsule (e.g., samples BPhE2 in Fig. 3a and 1010 in Fig. 3b), or frequently inside the platinum capsule for BPhE samples (see BPhE11 in Fig. S2A; see section 2.1 about temperature in BPhE experiments). Only for samples BPhE3 and BPhE10 was no such a bubble seen, but, for BPhE10, we surmise a bubble is located inside the platinum mass and was not revealed by the abrasion procedure, and, for BPhE3, pictures of the abraded capsule strongly suggest it was lost (Fig. 4b).

Reported partial melting experiments with carbonate-supplemented mafic compositions (Yaxley and Brey, 2004; Dasgupta et al., 2004, 2005, 2006; Gerbode and Dasgupta, 2010; Kiseeva et al., 2012) show that this type of assemblage is fully molten at 2-5 GPa and 1873 K if their initial CO_2 content is sufficiently high, i.e. > 5 wt.%. The silicate liquid formed at HT-HP, when CO_2-saturated, is expected to coexist either with a CO_2 vapor, or with a carbonatitic liquid immiscible with it, or both. On quenching, the silicate liquid transforms into glass with some crystallites, while the carbonatitic liquid, if present, tends to crystallize. This carbonatitic liquid must then be clearly visible in the texture of the run products as *crystallized* globules, features that we never saw in our samples. Therefore, in these experiments, we likely had a CO_2-bearing silicate liquid coexisting with a CO_2 supercritical fluid.

The frequently observed cavities must thus have been CO_2 bubbles at HP-HT. Care was exerted to check that these bubbles, when present, are located at the top of the capsule, and this was indeed found to be the case. For samples loaded with natural basalt, the carbonate powder was

initially placed at the bottom of the capsule, then covered by silicate material above it, and the bubble was yet systematically found at the top of the capsule. These CO_2 bubbles thus indicate that the samples were saturated with respect to CO_2 (as known for H_2O-bearing samples, e.g., Burnham and Jahns, 1962).

Samples and crystallites

When glass was obtained by quenching, the samples prepared from natural basalt appeared black, whereas the hand-prepared iron-free samples, turned out to be transparent, as expected. In some cases, the latter samples have a milky, whitish aspect indicating the presence of crystals in them.

For the whitish samples obtained using the Belt press (BPhE), a further analysis by scanning electron microscopy (SEM) reveals that the texture of most of them is essentially vitreous with the presence of extremely small crystallites of micron size. This is likely related to the relatively low quenching rate (section 2.1. above). When such crystallites are abundant enough, i.e., for pressures higher than 3 GPa, they may give a whitish general aspect, such as in BPhE11, where these crystallites have variable abundance throughout the sample, and are arranged in a way that generates several visible globules (Fig. S2a). From the SEM examination of BPHE11, the crystallites are silicate, and one can see that the globules are only regions with more abundant crystallites (Fig. S2b, magnification 2000).

For the samples obtained using the multi-anvil press, sample 1010 (5 GPa, 1873 K) is nicely vitreous, but samples 1090 (5 GPa, 1873 K) and 1011 (8.5 GPa, 1873 K) are partially crystallized. The latter two samples are discussed below (sections 3.3. and 3.4.).

Chemical composition of glass regions

The chemical composition, on a CO_2-free basis, of glass zones in samples retrieved after HP-HT experiments are close, but not identical, to those of the initial silicate blends (see Tables 1 and 2). The final dissolved CO_2 contents measured in the quenched samples are systematically lower than their initial concentrations. This corroborates the interpretation that bubbles were present in samples that were CO_2-saturated.

Raman mapping of CO_2

An advantage of Raman spectroscopy is to allow quantifying the distribution of CO_2 (CO_3^{2-}) throughout the sample at the micron scale. Such Raman mapping revealed that significant variations of CO_2 content may occur across samples. For those samples where such mapping was done, we calculate the average of the individual measurements, and it is these average concentrations that are reported in Table 2, with an uncertainty corresponding to the observed dispersion.

Appropriate values for global samples

Such mapping was performed on sample BPhE10, 2 GPa, with 19 Raman spots (see Fig. 4a), and revealed a strong heterogeneity in CO_2 concentrations from 0.29 to 2.37 wt.%, with an average value of 1.56±0.80 wt.%. Moreover, as can be seen on Fig. 4a, the CO_2 concentrations are

503 weak at the bottom of the capsule, although the carbonate powder was initially placed at the
504 bottom, and they increase toward the top (where we guess a cavity is perhaps located inside the
505 platinum, or the bubble was lost). This argues for a complete redistribution of CO_2 in the capsule
506 during the experiment.
507 The same systematics is observed for sample 1010 (5 GPa) from 12 Raman spots, giving less
508 variable CO_2 concentrations ranging between 5.03 and 6.94 wt.% and averaging 5.97±0.53 wt.%,
509 where Raman mapping reveals an increase of the CO_2 concentration towards the top of the capsule
510 where the bubble is located (Fig. 3b).
511 These samples have perhaps not reached equilibrium for CO_2. Sample BPhE10 remained 32
512 minutes at 2 GPa and 1920K, while sample 1010 spent 3 hours at 5 GPa and 1873K. Therefore, it
513 is likely that CO_2 concentrations are never homogeneous in such kind of samples but are variable
514 due to CO_2 migration driven by the exsolution process that generates the bubble. These
515 observations indicate that the kinetics of such CO_2 migration is slow in the experimental conditions
516 with respect to the duration of the experiments. That sample 1010 appears more homogeneous
517 than BPhE10 is probably due to the much longer duration of the experiment, 3 hours vs. 32
518 minutes.
519 For these durations, we can calculate the typical diffusion length of a carbonate ion in melt if we
520 know the diffusion coefficient, using the formula $x = \sqrt{6Dt}$. For sample 1010, using the value of 4
521 10^{-10} m^2/s for CO_3^{2-} in a MORB melt at 2 GPa and 1873 K from the simulations of Guillot and Sator
522 (2011, their Table 3), one gets 5 mm. At 5 GPa, the diffusion coefficient must be slightly smaller by
523 some tens of percent. However, these authors indicate that their values are probably
524 overestimated by a factor of 10. Their review of literature shows that the CO_2 molecular diffusion at
525 ambient pressure does not clearly depend on melt composition (see also Baker et al., 2005) and
526 that the data yields a linear trend in an Arrhenius plot (their figure 12). Extrapolating this trend to
527 1873 K gives a value of 7 10^{-11} m^2/s, which allows estimating a length of ~2 mm. For sample
528 BPhE10, at 1920K, we extrapolate to roughly the same value of the diffusion coefficient, and, in 32
529 minutes, the diffusion length is 0.9 mm. Given that our capsules are roughly 2 mm tall, these
530 calculations suggest that several hours may be necessary to reach CO_2 homogeneity in the melt.
531 It is also possible that the better homogeneity of sample 1010 compared to sample BPhE10
532 would be related to the higher cooling rate for the multi-anvil press than for the Belt press (section
533 2.1.), thus better freezing a possible re-solution of some gas from the bubble on cooling, but this is
534 yet too speculative.
535 The simplest way of interpreting these observations is probably to assume equilibrium at the
536 scale of the whole capsule between CO_2 dissolved in melt and CO_2 of the bubble, the melt being not
537 completely homogenized. It is thus probable that the values obtained for whole samples by
538 averaging several measurements are trustable only when the number of Raman spots is sufficient.
539 In contrast, sample BPhE3 (3 GPa) appears more homogeneous, with an average value of
540 4.21±0.25 wt.% CO_2, but we have only 6 spots for this sample (only 4 spots are shown on Fig. 4b).
541 This sample spent 33 minutes at 3 GPa and 2000K, thus it is possible that this apparent better
542 homogeneity is due to this higher temperature. We also remark that the relatively short duration of
543 the experiment here does not appear to have prevented homogeneity, hence probably equilibrium,
544 from being reached. However, given that we have only 6 points, it is still possible that zones with

lower or higher CO_2 concentrations have been missed, so that the average value for this sample is perhaps not accurate. But we shall see below that, compared to theoretical values obtained by molecular dynamics (section 4.1.), the result for BPhE3 is likely correct within experimental error.

Finally, the global values obtained for samples BPhE2 with 2 spots and BPhE12 with one measurement spot are possibly not accurate. Sample BPhE12 (1.5 GPa, 1825 K)) gives the same value within experimental error as reported previously by Mattey (1991) and by Stanley et al. (2011, 2012). This result is also consistent with the theoretical values. In contrast, sample BPhE2 (2 GPa, 1920 K) gives a clearly too high value when compared to previous results or to theory (see section 4).

3.2. Partially crystallized sample BPhE11 (4 GPa)

Sample BPhE11 (4 GPa and 2130 K) shows a large cavity inside the platinum at the top of the capsule. This sample is not completely vitreous, with whitish regions sometimes taking the form of globules (Fig. S2a). For this sample, SEM analysis shows that the global texture is that of a glass bearing very abundant silicate crystallites. Therefore, it is impossible to have the Raman spot located on pure glass, but it always includes some crystallites, which must lower the measured CO_2 concentration. Thus, for this sample, we selected only the highest CO_2 results, using them to obtain a rough value of its global CO_2 content (Table 2).

3.3. Partially crystallized sample 1090 (5 GPa)

The andesitic sample 1090, exposed to 5GPa, partially crystallized upon quenching (Fig. S6). Raman analysis showed that the phenocrysts are aragonite, the high-pressure high-temperature polymorph of $CaCO_3$ (Suito et al., 2001; Ivanov and Deutsch, 2002; Spivak et al., 2012), identified by the three low frequency peaks at 155, 180 and 205 cm^{-1} (lattice modes), and the narrow peaks at 700 and 1085 cm^{-1} (Fig. 5, to compare with Gillet et al., 1993). We found no spectral signatures revealing crystalline silicates or other carbonates. The aragonite crystals are dispersed throughout a vitreous silicate matrix (Fig. S6b) of dacitic-like composition (see microprobe analysis of vitreous regions in Table 2).

Mean CO_2 content from optical estimate of phenocryst proportion

We estimated the volume proportion, V_c (in vol.%), of aragonite phenocrysts from an optical photography of the whole sample (not shown). We found V_c = 18±2 vol.% (see supplement).

Deriving the corresponding CO_2 content needs knowledge of densities of aragonite and glass (see supplement). Using densities at ambient conditions yields a CO_2 content of 9±1 wt.%. It would perhaps be more appropriate to use density values effective during the quench, at higher pressure and higher temperature, but they are unknown. Furthermore, we did not consider any

possible deviation from the assumed identity between area proportion and volume proportion, 2D vs. 3D.

This rough evaluation neglects the CO_2 still dissolved in the vitreous regions of the sample. Nevertheless, the obtained value suggests that all the initial CO_2, i.e., 9 wt.% (Table 1), was dissolved in this andesitic melt at 5 GPa. This sample was thus CO_2-saturated or slightly undersaturated, consistent with the fact that no CO_2 bubble is seen in it (Fig. S6a).

Micrometric scale Raman mapping of groundmass

Crystallization of this sample prevents using Raman spectroscopy to determine its global CO_2 content. An estimate can be obtained by summing up the fraction of CO_2 in glass, determined with Raman data, with that found in aragonite crystals.

A Raman mapping at micrometric scale revealed that very small aragonite crystallites of less than a few microns are dispersed in the glass in most regions of sample 1090 (Fig. 5). Aragonite is characterized by sharp peaks at 155, 180, 205, 700 and 1085 cm^{-1}. Glass presents broad bands near 100, 500, 800, 1000 cm^{-1}, with the doublet assigned to dissolved CO_3^{2-} at 1300-1600 cm^{-1}, while the ν_1 stretching mode of dissolved CO_3^{2-} at 1085 cm^{-1} is buried under the silicate shoulder located at 1000-1200 cm^{-1}. The Raman signal of aragonite is thus superimposed to that of vitreous silicate (see the sharp 1085 cm^{-1} peak shown in green in the spectrum of the glass + crystallites mixture, Fig. 5).

We measured the area, named A_{1085}, of the CO_3^{2-} sharp peak seen in the glass + crystals mixture (Fig. 5), and the area, named $A_{1085}^{aragonite}$, of the same peak in a large aragonite crystal chosen in the sample. The ratio $R_{1085} = A_{1085}/A_{1085}^{aragonite}$ is then related to the CO_2 concentration borne by crystallites by a simple linear relation (see supplement) because the intensity of a vibration band is proportional to the concentration of vibrators per unit volume seen by the laser beam.

Averaged over a surface of 30 X 30 micrometers, this mapping gives R_{1085} = 0.1137. Using the relationship between R_{1085} and CO_2 concentration (see supplement), the derived mean CO_2 concentration in glass is 8.1 wt.%, this value representing the contribution of the aragonite crystallites.

Evaluation of CO_2 concentration in sample 1090

Two analyzes at very different scales, optical image analysis and Raman mapping (Fig. 5), give similar results, indicating that sample 1090 contains 8 to 9 wt.% CO_2. The optical analysis does not take into account the residual CO_2 dissolved in glass, which is revealed by the presence of the doublet at 1350-1600 cm^{-1}. In zones where no aragonite Raman signal is visible near 1085 cm^{-1}, the CO_3^{2-} vibration band of CO_2 dissolved in glass is completely masked by the intense and broad band of silicate in this frequency range (Fig. 5). As the total CO_2 content cannot be larger than the 9.0 wt.% of initial CO_2, the concentration of residual CO_2 in glass is at most equal to the difference 9.0 - 8.1 = 0.9 wt.%. If we use the Raman calibration line (Fig. 2) to get the corresponding Raman signal via Eq. (2) and report this value into the Raman spectrum of the glass (Fig. 5), we see that the corresponding dissolved CO_3^{2-} band at 1080-1090 cm^{-1} indeed cannot emerge from the large silicate shoulder. Consequently, the CO_2 concentration in glass cannot exceed 0.9 wt.%, and the

total CO_2 may be as large as the initial amount of 9.0 wt.%. We thus again reach the conclusion that sample 1090 is undersaturated or just saturated, in agreement with the absence of any bubble.

Altogether, the global CO_2 concentration is between 8.1 and 9.0 wt.%. We thus report an intermediate value of 8.5±0.9 wt.% in Table 2 for the bulk CO_2 of sample 1090.

3.4. Partially crystallized sample 1011 (8.5 GPa)

Basaltic sample 1011, exposed to 8.5 GPa, yields a quenched structure made of an intergrowth of silicate and carbonate crystals, with some proportion of glass (Fig. 6). To our knowledge, no report of pure glass obtained at such a high pressure exists for such compositions in the literature, so that high pressure likely just prevents from getting glass with a classical quenching procedure (quench rate ~100K/s).

A quick Raman mapping of this sample allows identifying garnets (grossular and mostly pyrope) and carbonates (Fig. 7), as well as glass regions dispersed throughout. In the spectra taken from glass regions, one can clearly distinguish the Raman shifts corresponding to the stretching modes of dissolved carbonate ions (see in Fig. 7 – glass, the broad band at ~1090 cm^{-1} and the doublet at 1350-1600 cm^{-1}) and those generated by solid carbonates (see in Fig. 7 – glass, the narrow peak at 1103 cm^{-1}). The narrow peak at 1103 cm^{-1}, instead of 1085 cm^{-1} in aragonite, is characteristic of the ν_1 stretching mode of CO_3^{2-} in mineral eitelite, $Na_2Mg(CO_3)_2$ (see Shatskiy et al., 2013). Indeed, the microprobe analyzes of glass regions reveals a strong enhancement of Na with respect to the initial composition (see Tables 1 and 2), suggesting that, during the quench, a large proportion of Na^+ ions migrated together with CO_3^{2-} ions to form eitelite crystals.

Sample 1011 does not show any bubble, indicating that CO_2 was mostly dissolved in melt at HP-HT, and generated carbonate minerals on quenching. Accordingly, this sample must have retained all the 13.6 wt.% CO_2 put in the capsule. A quick optical analysis of the picture presented in Fig. 6 with the protocol used for sample 1090 indicates that the area fraction of white parts (crystals) is of 23-24%, leading to CO_2 values close to 12 wt.%, assuming all crystals are eitelite. Considering the uncertainties in such an analysis (on densities, different crystalline phases, only one image was analyzed...), this result corroborates the fact that the initial 13.6 wt.% CO_2 was quantitatively dissolved at 8.5 GPa. Since we observe neither any evidence of a leak in the platinum capsule, nor any bubble in the bulk material, we can thus assume that the basaltic melt at 8.5 GPa and 1873 K can integrate 13.6 wt.% CO_2, still being not saturated.

4. Discussion

4.1. CO_2 solubility in basaltic and andesitic melts up to 8.5 GPa

Breaking of Henry's law at high pressure

The measured CO_2 contents of the studied samples globally exhibit a strong increase with increasing pressure (Fig. 8). Above 2 GPa, the CO_2 solubility in basaltic and andesitic melts increases much faster than what is expected from an extrapolation of the Henrian behavior known

at lower pressure (e.g. Pan et al., 1991; Mattey, 1991; Stanley et al., 2011, 2012). Deviations from Henry's law at high pressure have already been pointed out, for rare gases toward low solubility (Schmidt and Keppler, 2002; Sarda and Guillot, 2005; Guillot and Sarda, 2006; Bouhifd and Jephcoat, 2006), and for CO_2 toward high solubility but only on theoretical grounds (Guillot and Sator, 2011).

Comparison to previous data and accuracy of results

In detail, when compared to the seldom data reported in the literature for mafic compositions between 1 and 3 GPa (e.g., Pan et al., 1991; Mattey, 1991; Stanley et al, 2011, 2012; Eguchi and Dasgupta, 2017), our experimental results are compatible with Pan et al. (1991) and Stanley et al. (2011, 2012) at 1.5 GPa within error for sample BPhE12 (although slightly higher), and with Mattey (1991) and Stanley et al. (2011, 2012) at 2 GPa for sample BPhE10 (Fig. 8). We remark that the results of Stanley et al. (2011, 2012) are for iron-rich Martian-like basalt compositions and are slightly lower than ours but very close.

The experimental results of Eguchi and Dasgupta (2017) for andesite at 1-3 GPa are significantly lower than the rest of presently available data, but their experiments were conducted at graphite saturation and are therefore not comparable. Their thermodynamic model (Eguchi and Dasgupta, 2018) for CO_2 solubility in silicate melts fits relatively well the low-pressure data (Fig. S8), but as seen on Fig. 8, their curve goes down when pressure increases above ~5 GPa. In addition, their model appears quite sensitive to chemical composition (Fig. 8 and S7).

Our 2 GPa sample BPhE2 gives clearly a too high CO_2 concentration. As discussed above, the samples are heterogeneous, and we have not enough Raman spots for this sample so that the obtained result is likely too high (compare BPhE2 and BPHE10 in Table 2 and see Fig. 4a for BPhE10 at 2 GPa). The result for BPhE2 must thus be rejected and is not shown on Fig. 8. We keep the rest of our results as representative of the CO_2-P evolution at various temperatures (Fig. 8).

Finally, the result of Kim et al. (2018) at 6 GPa, although for albite melt, is ~15 wt.%, an extremely elevated value that agrees well with our measurements for basalt and andesite compositions. A comparison with simulation below allows appreciating this datum better.

4.2. Molecular dynamics approach

Simulation of CO_2 solubility in mafic melts

A number of solubility models have been proposed in the literature to describe the CO_2 solubility in silicate melts as function of pressure, composition, and (more recently) redox state (e.g., Khitarov and Kadik, 1973; Dixon et al., 1995, Papale et al., 2006, Iacono-Marziano et al., 2012, Eguchi and Dasgupta, 2018). These models being empirical in nature, their parameters cannot be a priori deduced and are adjusted to reproduce at best some solubility data set. When it comes to the question of applying these models to predict the carbon solubility for thermodynamic conditions and/or for silicate composition not spanned by the experimental data basis used for parametrization, the results are generally poor. In particular, most of these solubility models have been parametrized at relatively low pressure (< 2 GPa), and as shown hereafter, they are unable to reproduce the present HP experiments and disagree with the MD calculations. In contrast, MD

calculations are based on a first principles approach, and once the force field has been set up, no adjustment of parameters is needed to describe the CO_2 solubility in silicate melts of various composition at any thermodynamic conditions.

For having theoretical guidance in this study, we compare our data to the molecular dynamics simulation study published by two of us (for technical details, see Guillot and Sator, 2011). In Fig. 8 is reported the solubility of CO_2 in a MORB melt at 1673K, 1873K and 2273K as function of pressure, as calculated by MD, as well as that for an andesitic melt at 1873K. The general trend predicted by the MD calculation, a strongly nonlinear increase of solubility at high pressure, is supported by present experimental data, which also supports the validity of Raman spectroscopy as a measurement technique of CO_2 concentration in silicate material (Fig. 8).

Using MD simulations to discuss Raman CO_2 results

The theoretical lines we have, permit to discuss the accuracy of the measured values.

At 1.5 GPa and 1820K, sample BPhE12 gives a value slightly higher than, but consistent with those of Pan et al. (1991) and Stanley et al. (2011, 2012) within error. Our value is also consistent with the simulations within error, but slightly high (Fig. 8 and S7). This sample was perhaps relatively homogeneous, but again, had only one Raman measurement spot.

At 2 GPa and 1920K, sample BPhE2 gives clearly a too high value (not shown on Fig. 8), while sample BPhE10, at the same pressure and temperature, gives a result perfectly consistent with Mattey (1991), Stanley et al. (2011, 2012) and the MD lines at 1673 – 2273K (Fig. 8). Sample BPhE2 is rejected due to sample heterogeneity having not been measured, 2 measurement points versus 19 points).

At 3 GPa, sample BPhE3 was heated at ~2000 K and turns out to be quite homogeneous, which may be due to the temperature, higher than for BPhE2 and BPhE10 by ~100K. It gives a value consistent, within error, with the MD line at 1873K, which supports the validity of this experimental result (Fig. 8 and S7).

At 4 GPa and 2130K, sample BPhE11, although partially crystallized, gives a value consistent with the MD line at 2273K, supporting the significant effect of the high temperature in lowering the CO_2 solubility seen by MD (Fig. 8).

At 5 GPa and 1873K, the haplo-basaltic sample 1010 gives a value that is consistent, within error, with the MD line at 2273K for MORB, but relatively low for a MORB at 1873K. In the same (P,T) conditions, the haplo-andesite 1090 gives a value perfectly consistent within error with the MD line for an andesite at 1873K (Fig. 8).

AT 8.5 GPa and 1873K, the undersaturated sample 1011 accommodates 13.6 wt.% CO_2, the maximum possible, a value that does not contradict the MD result of ~25 wt.% for a saturated MORB at 1873K (Fig. 8).

The global agreement between data and simulation thus suggests that the CO_2 solubility curve in basaltic and andesitic melts is well constrained up to 5 GPa, and, based on sample 1011, probably up to 8.5 GPa. The strong increase in CO_2 solubility above ~2 GPa is confirmed.

The consistency of the result by Kim et al. (2018) for albite melt with our results and simulations (Fig. 8) further supports these conclusions.

4.3. Influence of melt composition

Molecular vs. ionic solubility

Comparing results for samples 1090 (5 GPa, 1873 K) and 1010 (same P, T) shows that the solubility of CO_2 in a haploandesitic melt is similar to that in a haplobasaltic composition in these conditions (Fig. 8). To check whether this observation holds over a large pressure range, we have evaluated by MD simulation the CO_2 solubility curve at 1873K, from 1 to 10 GPa, in a silicate liquid having the andesitic composition of sample 1090 (the force field, MD code and simulation parameters are those used in Guillot and Sator (2011): the obtained solubility curve for andesite is quite close to but slightly below that for MORB (Fig. 8). This similarity is due to a subtle energy-entropy compensation when CO_2 is incorporated into a silicate melt (Guillot and Sator, 2011). In polymerized melts, the number of NBO (non-bridging oxygen atoms) is too low to stabilize an important fraction of carbonate groups, but the work to spend for inserting a CO_2 molecule into the silicate network is weaker than in depolymerized melts because of a less compact structure. Therefore, the CO_2 solubility is similar in basalt and andesite at 1873 K, and the MD calculation takes this feature into account.

We note that this result contradicts several previous studies performed at lower pressure, where it was observed that the CO_2 solubility was significantly higher in basalt than in andesite (e.g., Mysen, 1976; Dixon, 1997; Brooker et al., 1999, 2001a,b; King et Holloway, 2002; Lesne et al., 2011; Iacono-Marziano et al., 2012), increasing with increasing NBO/T (here T means the number of tetracoordinated elements Si and Al). Of course, we do not claim that there is no influence of the NBO/T, i.e., chemical composition, but things are probably subtler at high T and P because of the interplay of carbonate ions and molecular CO_2, the solubility of which are extremely sensitive to experimental conditions (T, P and H_2O content).

The experimental results are possibly influenced by changes occurring during quenching, where cooling could trigger CO_2 conversion into CO_3^{2-}, a phenomenon already experimentally documented (Morizet et al., 2002; Nowak et al., 2004; Konschak and Keppler, 2014) and theoretically described by Guillot and Sator (2011). Konschak and Keppler (2014) show that this speciation effect is much stronger for depolymerized melts and strongly increases at low temperature, especially close to the glass transition temperature, T_g. Therefore, it appears important that future experiments rather attempt to perform measurements *in situ* at high pressure and high temperature.

Relation to melt properties and solvation structure.

We saw above that CO_2 solubility in basaltic and andesitic melt can reach similar and high values. However, such high amounts of dissolved CO_2 only slightly lower the glass transition temperature (T_g) of silicate melts (an example of such data is illustrated in Fig. S8) or their viscosity (not shown; e.g., Bourgue and Richet, 2001; Morizet et al., 2002; Di Genova et al., 2014), the effect on viscosity being, as expected, essentially visible close to T_g, when viscosity is high enough (Bourgue and Richet, 2001). In contrast, solubilization of water (Richet et al., 1996; Vetere et al., 2006; Whittington et al., 2000) or Na_2O (Poole, 1949; Neuville, 2006; Le Losq et al., 2019) has a much stronger influence on both properties (Fig. S8). In addition, the CO_2 solubility is significantly lower than that of H_2O by one order of magnitude (e.g., Papale et al., 2006).

This weak influence of CO_2 on melt properties can be explained as follows (Guillot and Sator, 2011). Upon dissolution in a liquid silicate, a significant fraction of CO_2 turns into carbonate ion by linking to available non-bridging oxygen atoms, a smaller fraction links to bridging oxygen atoms without breaking the two Si-O bonds (contrary to H_2O), and the rest, a non-negligible fraction of it, finds interstitial sites where it stabilizes as a molecule, the higher the degree of polymerization the larger the fraction of molecular CO_2. In short, CO_2 links to the network as a parasite, without disturbing it.

In Raman spectra of the present study, the Raman band at ~1080 cm^{-1} is the signature of the solvation structure of the CO_3^{2-} ion in the silicate network. Indeed, as seen in Fig. 1.b, the frequency of this band is 1046 cm^{-1} in the KS samples, as compared to 1084-1086 cm^{-1} in the basaltic and andesitic samples: this is due to the different way the CO_3^{2-} ion links to these different silicate networks. In the same way, we notice a slight frequency change at 5 GPa between andesite and basaltic composition. However, for basaltic glasses, we do not observe any change in this frequency with changing pressure, which suggests that the solvation structure of the carbonate ion is essentially the same, whatever the pressure up to 8 GPa.

4.5. Consequences for CO_2 geochemistry

We present here an open tentative list of domains where our findings about high CO_2 solubility in melts with compositions close to (as possibly close as) natural mafic melts may be important. We discuss only few of them.

Mantle melting, volcanism, carbonatites and kimberlites

The present work may have consequences on our understanding of the transport of CO_2 at depth in the mantle, and hence of Earth degassing as a whole. One of them concerns mantle melting. When incipient melting occurs in the carbonate-bearing asthenosphere, at very low melt fraction ($\leq 0.1\%$), the initial composition of the melt is carbonatitic (e.g., Dasgupta and Hirschmann, 2006; Hammouda and Keshav, 2015) and it then evolves toward a basaltic composition during magma ascent and increasing silicate melting.

If basaltic-like magmas can carry so much carbon, this is probably another piece of evidence in favor of continuity between pure silicate melt and pure carbonate melt (see e.g., Gudfinnsson and Presnall, 2005). During magma ascent toward the surface, carbonate and silicate melt will likely separate when conditions for immiscibility are met (e.g., Fischer et al. 2009), thus leading to a carbonatitic melt again with probably some silicate dissolved in it, and a silicate melt significantly charged in dissolved CO_2 (for a scenario of magma ascent, see Gaillard et al., 2020).

The increase in melt fraction during melting must eventually induce a decrease in CO_2 concentration. After separation, the resulting silicate-rich melt will have a CO_2 concentration determined by the evolution of the CO_2 solubility with melt composition and pressure during melting. We show that basaltic magmas can transport high quantities of CO_2 (several wt.%) before degassing. For instance, at 8.5 GPa our data show that a basaltic melt is able to accommodate more than 13.6 wt.% CO_2 before starting degassing and as shown in Fig. 8, probably ~25wt.% (Guillot and Sator, 2011). We speculate that, if such melts could be generated at such high pressures and migrate up to the surface, their degassing could lead to explosive eruptions.

There is many evidence for a deep-sea explosive volcanism on the oceanic crust characterized by pyroclastic deposits with very high vesicularity or showing CO_2-rich melt inclusions (e.g., Schminke et al., 1978; Smith and Batiza, 1989; Hekinian et al., 2000; Pineau et al., 2004; Sohn et al., 2008; Helo et al., 2011). A part of these explosive episodes could be triggered by CO_2-rich magmas reaching CO_2 saturation in the pressure range 1-5 GPa (Aubry et al., 2013).

Other occurrences of CO_2-rich volcanism include, for example, the *petit spots*, a large number of oceanic submarine volcanoes, which appear on the ocean floor close to subduction zones (Hirano et al., 2013). These volcanoes were shown by Okumura and Hirano (2013) to erupt lavas as rich as 5 to 10 wt.% CO_2. These authors estimate they carry a flux of CO_2 out of the Earth of 0.6 to 1.2 10^{10} mole CO_2/year, a significant fraction of the MOR CO_2 degassing flux of 1-5 10^{12} mole CO_2/year (Dasgupta & Hirschmann, 2010). This flux may be higher when considering degassing not related to eruptions.

Another consequence of such high CO_2 solubility in silicate magmas at high pressure may be the occurrence of CO_2-rich fluids in the relatively shallow mantle, as witnessed by the numerous CO_2-H_2O fluid inclusions found in peridotite minerals (Frezzotti and Touret , 2014), possibly a record of a general, unfocussed, mantle CO_2 continuous degassing.

Altogether, the CO_2 flux from the interior of the Earth to the atmosphere may well be more important than several previous estimates, when considering (i) the high end of estimates for the Mid-Oceanic Ridge flux of 5-6 10^{12} mole/year, in full agreement with popping rocks (e.g., Sarda and Graham, 1990; Dasgupta and Hirschmann, 2010), (ii) the flux coming via the large number of petit spots and their degassing (Okumura and Hirano, 2013) and (iii) the general continuous mantle degassing (Frezzotti and Touret, 2014). Such CO_2 has not yet been directly identified, and part of it may be released via deep-sea hydrothermal activity.

About the carbonate melt possibly generated by immiscibility during ascent, it may play a role in the genesis of carbonatites and kimberlites, since such a melt will inevitably rise upward in the mantle (e.g., Russell et al., 2012; Kamenetsky and Yaxley, 2015), but this subject is still debated, and is beyond the scope of the present work.

Core-mantle boundary

Finally, let us recall that the D" zone, at the bottom of the mantle, may include liquid remnants of the primordial magma ocean (Williams and Garnero., 1996; Vinnik et al., 1998; Labrosse et al., 2007; Coltice et al., 2011). Although at much higher pressure than in this study, if we extrapolate the logic evidenced here, we speculate that such melt might contain high amounts of CO_2. Therefore, carbon may also play an important role in very deep mantle processes, such as in mantle – core interactions occurring in the D" zone. This could also relate to carbon being one of the light elements having entered the core when it formed (e.g., Wood, 1993; Poirier, 1994; Blanchard et al., 2015; Solomatova et al., 2019), a possibility supported by carbon being found as carbide in some iron meteorites (Scott, 1971). Clearly, data at higher pressures should be generated to follow-on the solubility curves of Fig. 8 and contribute to answer the question of CO_2-rich melts existing at such great depths, a challenge for the future.

6. Conclusion

New data have been acquired on the solubility of CO_2 in silicate melts close to basaltic and andesitic compositions at pressures up to 8.5 GPa in oxidizing conditions. Although the solubility of CO_2 in such melts is weak at low pressures (500-1,000 ppmw at 1 kbar, Dixon et al., 1995; Botcharnikov et al., 2006), our data show that it increases with increasing pressure much more rapidly than expected from Henry's law (e.g., C_{CO_2} = 7-8 wt.% at 5 GPa as compared to 2.5-3 wt.% from Henry's law), confirming previous inferences from theoretical work (e.g., Guillot and Sator, 2011). At 8.5 GPa, we obtain a minimum CO_2 concentration of 13.6 wt.% as compared to ~25 wt.% from molecular dynamics. That such silicate melts may contain such high amounts of CO_2 may have important consequences on our understanding of CO_2 transport at depth in the mantle, such as when mantle melts in the asthenosphere, and, more globally, our understanding of Earth degassing, especially at the magma ocean stage. Other consequences are tentatively suggested, such as about the origin of carbonatites or kimberlites, and about the core – mantle boundary.

From the experimental point of view, the present study highlights the usefulness of Raman spectroscopy for analyzing silicate glasses in a quick and non-destructive fashion. Quantification of CO_2 is possible in glasses, does not depend on acquisition conditions and glass composition, and as suggested by comparison with existing studies, on the type of Raman spectrometer.

A major problem of the experimental method used in this study is to deal with a sample issued from quenching the liquid phase, which has therefore experienced undesirable structural changes (crystallites) and possible chemical variations. As seen here, a mixture of silicate and carbonate exposed to pressures above 5 GPa is unlikely to quench to pure glass. Moreover, the establishment of an equilibrium between silicate liquid and CO_2 gas was observed here to produce significant heterogeneities of the CO_2 concentration in the silicate liquid observed as a quench. We thus believe that a breakthrough in this field will arise from *in situ* spectroscopies running at superliquidus temperatures and high pressure.

Acknowledgements

This project was made possible thanks to funding by the French CNRS via a "delegation" to the Laboratoire des Sciences de la Terre, UMR-CNRS 5570, of ENS-Lyon. Ph. S. thanks his colleagues at Orsay University, who took charge of his teaching over two years. We are very much indebted to the the High Pressure platform, ILMTech-PLECE, headed by Prof. Alfonso San Miguel, who kindly allowed Ph.S. and E.C. using the Belt-type press at Université Claude Bernard - Lyon 1. We warmly thank Pierre Toulemonde and Sylvie Le Floch, at Lyon 1, for their help with the Belt press and with preparation of assemblies, as well as Hervé Ferret for his help at making lots of pieces for the assemblies. We also wish to thank Ken Koga for helpful discussions about the design of the assembly for the Belt press. We thank very much the French CNRS-INSU for access to the Multi-Anvil Press national facility in Clermont-Ferrand. N.S. and B.G. acknowledge funding from ANR, 2010-BLAN-621-03) and ERC (n° 279790). Also, thanks to Jean-Guy Schilling who agreed to let us use an EW9309 MORB sample for HP experiments.

921

References:

Amalberti J., Neuville D.R., Sarda P., Sator N. and Guillot B., 2011a. Quantification of CO_2 dissolved in silicate glasses and melts using Raman spectroscopy: Implications for geodynamics, Mineral. Mag. 75, Goldschmidt Abstracts 2011, p. 430.

Amalberti J., Neuville D.R., Sarda P., Sator N. and Guillot B., 2011b. Quantification of CO_2 dissolved in silicate glasses and melts using Raman spectroscopy: Implications for geodynamics, Japan Geoscience Union Meeting 2011.

Aubry G.J., Sator N. and Guillot B., 2013. Vesicularity, bubble formation and noble gas fractionation during MORB degassing, Chem. Geol. 343, 85-98. https://doi.org/10.1016/j.chemgeo.2013.02.006

Baker D. R., Freda C., Brooker R. A. and Scarlato P., 2005. Volatile diffusion in silicate melts and its effects on melt inclusions. Ann. Geophys. 48, 699–717. DOI:10.4401/AG-3227

Ballentine C.J., O'Nions R.K., Oxburgh E.R., Horvath F. and Deak J., 1991. Rare gas constraints on hydrocarbon accumulation, crustal degassing and groundwater flow in the Pannonian Basin, Earth Planet. Sci. Lett. 105, 229-246. https://doi.org/10.1016/0012-821X(91)90133-3

Ballentine C.J., 1997. Resolving the mantle He/Ne and crustal 21Ne/22Ne in well gases, Earth Planet. Sci. Lett. 152, 233-249. https://doi.org/10.1016/S0012-821X(97)00142-8

Behrens H., Ohlhorst S., Holtz F. and Champenois M., 2004. CO_2 solubility in dacitic melts equilibrated with H_2O-CO_2 fluids: Implications for modeling the solubility of CO_2 in silicic melts. Geochim. Cosmochim. Acta 68, 4687-4703. doi:10.1016/j.gca.2004.04.019

Behrens H., Roux J., Neuville D.R. and Siemann M., 2006. Quantification of dissolved H_2O in silicate glasses using confocal Raman spectroscopy. Chem. Geol. 229, 96–112. DOI:10.1016/j.chemgeo.2006.01.014

Bézos A. and Humler E., 2005. The $Fe^{3+}/\Sigma Fe$ ratios of MORB glasses and their implications for mantle melting, Geochim. Cosmochim. Acta 69, 711–725. DOI:10.1016/j.gca.2004.07.026

Blanchard I., Badro J., Siebert J. and F.J. Ryerson, 2015. Composition of the core from gallium metal-silicate partitioning experiments. Earth Planet. Sci. Lett. 427, 191-201. https://doi.org/10.1016/j.epsl.2015.06.063

Blank J.G. and Brooker R.A., 1994. Experimental studies of carbon dioxide in silicate melts: Solubility, speciation, and stable carbon isotope behavior. Rev. Mineral. Geochem. 30, 157-186. https://doi.org/10.1515/9781501509674-011

Botcharnikov, R.E., Freise, M., Holtz, F., Behrens, H., 2005a. Solubility of C–O–H mixtures in natural melts: new experimental data and application range of recent models. Annals of Geophysics 48, 633–646. DOI: https://doi.org/10.4401/ag-3224

Botcharnikov R.E., Behrens H. and Holz F., 2006. Solubility and speciation of C-O-H fluids in andesitic melt at T= 1100-1300°C and P=200 and 500 MPa. Chem. Geol. 229, 125-143. DOI:10.1016/j.chemgeo.2006.01.016

Bouhifd M.A. and Jephcoat A.P., 2006. Aluminium control of argon solubility in silicate melts under pressure. Nature 439, 961–964. DOI:10.1038/nature04583

Bourgue E. and Richet P., 2001. The effects of dissolved CO_2 on the density and viscosity of silicate melts: a preliminary study. Earth Planet. Sci. Lett. 193, 57-68. https://doi.org/10.1016/S0012-821X(01)00491-5

964 Brawer S.A. and White W.B., 1975. Raman spectroscopic investigation of the structure of silicate
965 glasses. (I) The binary alkali silicates. J. Chem. Phys. 63(6), 2421-2432.
966 https://doi.org/10.1063/1.431671
967 Brawer S.A. and White W.B., 1977. Raman spectroscopic investigation of the structure of silicate
968 glasses. (II) Soda-alkaline earth-alumina ternary and quaternary glasses. J. Non-Crystal. Solids
969 23(2), 261-278. https://doi.org/10.1016/0022-3093(77)90009-6
970 Brooker R.A., Kohn S.C., Holloway J.R., McMillan P.F. and Carroll M.R., 1999. Solubility, speciation
971 and dissolution mechanisms for CO_2 in melts on the Na-AlO_2-SiO_2 join. Geochim. Cosmochim.
972 Acta 63, 3549-3565. https://doi.org/10.1016/S0016-7037(99)00196-9
973 Brooker R.A., Kohn J.R., Holloway J.R. and McMillan P.F., 2001a. Structural controls on the
974 solubility of CO2 in silicate melts: Part I: Bulk solubility data. Chem. Geol. 174, 225-239.
975 DOI:10.1016/S0009-2541(00)00353-3
976 Brooker R.A., Kohn J.R., Holloway J.R. and McMillan P.F., 2001b. Structural controls on the
977 solubility of CO_2 in silicate melts: Part II: IR characteristics of carbonate groups in silicate
978 glasses. Chem. Geol. 174, 241-254. https://doi.org/10.1016/S0009-2541(00)00318-1
979 Brooker R.A., Sparks R.S.J., Kavanagh J.L. and Field M., 2011. The volatile content of hypabyssal
980 kimberlite magmas: some constraints from experiments on natural rock compositions. Bull.
981 Volcanol. 73, 959-981. DOI:10.1007/s00445-011-0523-7
982 Burke E.A.J. and Lustenhouwer W.J., 1987. The application of a multichannel laser Raman
983 microprobe (Microdil-28®) to the analysis of fluid inclusions. Chem. Geol. 61, 11-17.
984 https://doi.org/10.1016/0009-2541(87)90021-0
985 Burnham C.W. and Jahns R.H., 1962. A method for determining the solubility of water in silicate
986 melts. Am. J. Sci. 260(10), 721-745. DOI:10.2475/ajs.260.10.721
987 Cameron A.G.W., 1973. Abundances of the elements in the solar system. Space Sci. Rev. 15, 121-
988 146. https://doi.org/10.1007/BF00172440
989 Capriolo M., Marzoli A., Aradi L.E., Callegaro S., Dal Corso J., Newton R. J., Mills B. J.W., Wignall P.
990 B., Bartoli O., Baker D. R., Youbi N., Remusat L., Spiess R. and Szabó C., 2020. Deep CO_2 in the
991 end-Triassic Central Atlantic Magmatic Province. Nat. Commun. 11, 1670.
992 https://doi.org/10.1038/s41467-020-15325-6
993 Chabiron A., Pironon J. and Massare D., 2004. Characterization of water in synthetic rhyolitic
994 glasses and natural melt inclusion by Raman spectroscopy. Contrib. Mineral. Petrol. 146, 485–
995 492. DOI:10.1007/s00410-003-0510-x
996 Chavrit D., Humler E., Grasset O., 2014. Mapping modern CO_2 fluxes and mantle carbon content all
997 along the mid-ocean ridge system, Earth Planet. Sci. Lett. 387, 229–239.
998 https://doi.org/10.1016/j.epsl.2013.11.036
999 Chevrel M.O., Platz T., Hauber E., Baratoux D., Lavallée Y. and Dingwell D.B., 2013. Lava flow
1000 rheology: A comparison of morphological and petrological methods. Earth Planet. Sci. Lett. 384,
1001 109-120. http://dx.doi.org/10.1016/j.epsl.2013.09.022
1002 Chi H., Dasgupta R., Duncan M. and Shimizu N., 2014. Partitioning of carbon between Fe-rich alloy
1003 melt and silicate melt in a magma ocean – Implications for the abundance and origin of volatiles
1004 in Earth, Mars, and the Moon. Geochim. Cosmochim. Acta 139, 447–471.
1005 https://doi.org/10.1016/j.gca.2014.04.046

1006 Cochain B., Neuville D.R., Henderson G. S., McCammon C. A., Pinet O. and P. Richet, 2012. Effects
1007 of the iron content and redox state on the structure of sodium borosilicate glasses: A Raman,
1008 Mössbauer and Boron K-Edge XANES spectroscopy study. J. Am. Ceram. Soc. 95, 962-971.
1009 DOI:10.1111/j.1551-2916.2011.05020.x
1010 Coltice N., Moreira M., Hernlund J. and Labrosse S., 2011. Crystallization of a basal magma ocean
1011 recorded by Helium and Neon. Earth. Planet Sci. Lett. 308, 193-199.
1012 doi:10.1016/j.epsl.2011.05.045
1013 Craven P. and Wahba G., 1979. Smoothing noisy data with spline functions. Numer. Math. 31, 377-
1014 403. https://doi.org/10.1007/BF01404567
1015 Dasgupta R., Hirschmann M.M. and Withers A.C., 2004. Deep global cycling of carbon constrained
1016 by the solidus of anhydrous, carbonated eclogite under upper mantle conditions. Earth Planet.
1017 Sci. Lett. 227, 73-85. DOI:10.1016/j.epsl.2004.08.004
1018 Dasgupta R., Hirschmann M.M. and Dellas N., 2005. The effect of bulk composition on the solidus
1019 of carbonated eclogite from partial melting experiments at 3GPa. Contrib. Mineral. Petrol. 149,
1020 288-305. DOI:10.1007/s00410-004-0649-0
1021 Dasgupta R. and Hirschmann M.M., 2006. Melting in the Earth's deep upper mantle caused by
1022 carbon dioxide. Nature 440, 659-662. https://doi.org/10.1038/nature04612
1023 Dasgupta R., Hirschmann M.M. and Stalker K., 2006. Immiscible transition from carbonate-rich to
1024 silicate-rich melts in the 3 GPa melting interval of eclogite + CO_2 and genesis of silica-
1025 undersaturated ocean-island lavas. J. Petrol. 47, 647-671. https://doi.org/10.1093/
1026 petrology/egi088
1027 Dasgupta R. and Hirschmann M.M., 2010. The deep carbon cycle and melting in Earth's interior.
1028 Earth Planet. Sci. Lett. 298, 1-13. DOI:10.1016/j.epsl.2010.06.039
1029 Di Genova D., Romano C., Alletti M., Misiti V. and Scarlato P., 2014. The effect of CO_2 and H_2O on
1030 Etna and Fondo Riccio (Phlegrean Fields) liquid viscosity, glass transition temperature and heat
1031 capacity. Chem. Geol. 377, 72-86. https://doi.org/10.1016/j.chemgeo.2014.04.001
1032 Dixon J.E., 1997. Degassing of alkalic basalts. Am. Mineral. 82, 368-378.
1033 https://doi.org/10.2138/am-1997-3-415
1034 Dixon J.E., Stolper E.M. and Holloway J.R., 1995. An experimental study of water and carbon
1035 dioxide solubilities in mid-ocean ridge basaltic liquids. Part I: calibration and solubility models. J.
1036 Petrol. 36, 1607-1631. https://doi.org/10.1093/oxfordjournals.petrology.a037267
1037 Douglass J., Schilling J.-G. and Fontignie D., 1999. Plume-ridge interactions of the Discovery and
1038 Shona mantle plumes with the southern Mid-Atlantic Ridge (40°-55°S). J. Geophys. Res. 104,
1039 2941-2962. DOI:10.1029/98JB02642
1040 Dufils Th., Folliet N., Mantisi B., Sator N. and Guillot B., 2017. Properties of magmatic liquids by
1041 molecular dynamics simulation: The example of a MORB melt. Chem. Geol. 461, 34-46.
1042 http://dx.doi.org/10.1016/j.chemgeo.2016.06.030
1043 Eggler D.H., 1976. Does CO_2 cause partial melting in the low-velocity layer of the mantle? Geology
1044 4, 69-72. DOI:10.1130/0091-7613(1976)4<69:DCCPMI>2.0.CO;2
1045 Eguchi J. and Dasgupta R., 2017. CO_2 content of andesitic melts at graphite-saturated upper
1046 mantle conditions with implications for redox state of oceanic basalt source regions and
1047 remobilization of reduced carbon from subducted eclogite. Contrib. Mineral. Petrol. 172:12.
1048 DOI:10.1007/s00410-017-1330-8

Eguchi J. and Dasgupta R., 2018. A CO_2 solubility model for silicate melts from fluid saturation to graphite or diamond saturation. Chem. Geol. 487, 23-38. https://doi.org/10.1016/j.chemgeo.2018.04.012

Elkins-Tanton L., 2012. Magma oceans in the inner solar system, Annu. Rev. Earth Planet. Sci. 40, 113–139. DOI:10.1146/annurev-earth-042711-105503

Fischer T. P., Burnard P., Marty B., Hilton D. R., Füri E., Palhol F., Sharp Z. D. and Mangasini F., 2009. Upper-mantle volatile chemistry at Oldoinyo Lengai volcano and the origin of carbonatites. Nature 459, 77–80. DOI:10.1038/nature07977

Frezzotti M-L. and Touret J. L. R., 2014. CO_2, carbonate-rich melts, and brines in the mantle. Geoscience Frontiers 5, 697-710. http://dx.doi.org/10.1016/j.gsf.2014.03.014

Gaillard F., Sator N., Gardés E., Guillot B., Massuyeau M., Siffré D., Hammouda T. and Richard G., 2020. The link between physical and chemical properties of carbon-bearing melts and their application for geophysical image of Earth's mantle. In: Deep carbon past: to present, B. N. Orcutt, I. Daniel and R. Dasgupta eds., Cambridge University Press, 163-187. DOI: 10.1017/9781108477499

Galeener F. L. and Sen P. N., 1978. Theory of the first-order vibrational spectra of disordered solids. Phys. Rev. B 17(4), 1928-1933. DOI:10.1103/PhysRevB.17.1928

Genge M., Price G.D. and Jones A.P., 1995. Molecular dynamics simulations of CaCO, melts to mantle pressures and temperatures: implications for carbonatite magmas. Earth. Planet. Sci. Lett. 131, 225-238. doi.org/10.1016/0012-821X(95)00020-D

Gerbode C. and Dasgupta R., 2010. Carbonate-fluxed melting of MORB-like pyroxenite at 2.9 GPa and genesis of HIMU ocean island basalts. J. Petrol. 51, 2067-2088. https://doi.org/10.1093/petrology/egq049

Gerin, C., Gautheron, C., Oliviero, E., Bachelet, C., Djimbi, D. M., Seydoux-Guillaume, A. M., Tassan-Got, L., Sarda, P., Roques, J., and Garrido, F.: Influence of vacancy dam- age on He diffusion in apatite investigated at atomic to min- eralogical scales, Geochim. Cosmoch. Acta, 197, 87–103, https://doi.org/10.1016/j.gca.2016.10.018, 2017.

Gerlach T.M. and Nordlie B.E., 1975. The COHS gaseous system: Part I. Composition limits and trends in basaltic glasses. Am. J. Sci. 275, 353-376. DOI:10.2475/ajs.275.4.353

Gillet P., Biellmann C., Reynard B. and McMillan P., 1993. Raman spectroscopic studies of carbonates. Part I: High-pressure and High-temperature behavior of calcite, magnesite, dolomite and aragonite. Phys. Chem. Min. 20, 1-18. DOI:10.1007/BF00202245

Green D.H., Hibberson W.O., Kovacs I. and Rosenthal A., 2010. Water and its influence on the lithosphere-asthenosphere boundary. Nature 467, 448-451. DOI: 10.1038/nature09369

Grewal D.S., Dasgupta R., Sun C., Tsuno K. and Costin G., 2019. Delivery of carbon, nitrogen, and sulfur to the silicate Earth by a giant impact, Sci. Adv. 5, eaau3669. DOI: 10.1126/sciadv.aau3669

Gudfinnsson G.H. and Presnall D.C., 2005. Continuous gradations among primary carbonatitic, kimberlitic, melilititic, basaltic, picritic, and komatiitic melts in equilibrium with garnet lherzolite at 3-8 GPa. J. Petrol. 46, 1645-1659. DOI:10.1093/petrology/egi029

Gudmundsson G. and Holloway J.R., 1993. Activity-composition relationships in the system Fe-Pt at 1300 and 1400°C and at 1 atm and 20 kbar. Am. Mineral. 78, 178-186.

1091 Guillot B. et Sarda P., 2006. The effect of compression on noble gas solubility in silicate melts and
1092 consequences for degassing at mid-ocean ridges. Geochim. Cosmochim. Acta 70, 1215-1230.
1093 DOI:10.1016/j.gca.2005.11.007
1094 Guillot B. and Sator N., 2007a. A computer simulation study of natural silicate melts. Part I: low
1095 pressure properties. Geochim. Cosmochim. Acta 71, 1249–1265. doi:10.1016/j.gca.2006.11.015
1096 Guillot B. and Sator N. (2007b) A computer simulation study of natural silicate melts. Part II: high
1097 pressure properties. Geo- chim. Cosmochim. Acta 71, 4538–4556.
1098 Guillot B. and Sator N., 2011. Carbon dioxide in silicate melts: A molecular dynamics simulation
1099 study. Geochim. Cosmochim. Acta 75, 1829-1857. DOI:10.1016/j.gca.2011.01.004
1100 Hammouda T., 2003. High-pressure melting of carbonated eclogite and experimental constraints
1101 on carbon recycling and storage in the mantle. Earth Planet. Sci. Lett. 214, 357-368.
1102 DOI:10.1016/S0012-821X(03)00361-3
1103 Hammouda T. and Keshav S., 2015. Melting in the mantle in the presence of carbon: Review of
1104 experiments and discussion on the origin of carbonatites. Chem. Geol. 418, 171–188.
1105 https://doi.org/10.1016/j.chemgeo.2015.05.018
1106 Hamano K., Abe Y. and Genda H., 2013. Emergence of two types of terrestrial planet on
1107 solidification of magma ocean. Nature 497, 607-611. DOI:10.1038/nature12163
1108 Hekinian R., Pineau F., Shilobreeva S., Bideau D., Gracia E. and Javoy M., 2000. Deep sea
1109 explosive activity on the Mid-Atlantic Ridge near 34°50'N: Magma composition, vesicularity and
1110 volatile content. J. Volcanol. Geotherm. Res. 98, 49-77. https://doi.org/10.1016/S0377-
1111 0273(99)00190-0
1112 Helo C., Longpré M.-A., Shimizu N., Clague D.A. and Stix J., 2011. Explosive eruptions at mid-
1113 ocean ridges driven by CO_2-rich magmas. Nature Geoscience 4, 260-263.
1114 DOI:10.1038/NGEO1104
1115 Hirano N., Machida S., Abe N., Morishita T., Tamura A. and Arai S., 2013. Petit-spot lava fields off
1116 the central Chile trench induced by plate flexure. Geochem. J. 47, 249–257.
1117 https://doi.org/10.2343/geochemj.2.0227
1118 Iacono-Marziano G., Morizet Y., Le Trong E. and Gaillard F., 2012. New experimental data and
1119 semi-empirical parameterization of H_2O-CO_2 solubility in mafic melts. Geochim. Cosmochim.
1120 Acta 97, 1-23. https://doi.org/10.1016/j.gca.2012.08.035
1121 Ivanov B.A. and Deutsch A., 2002. The phase diagram of $CaCO_3$ in relation to shock compression
1122 and decomposition. Phys. Earth Planet. Int. 129, 131-143. https://doi.org/10.1016/S0031-
1123 9201(01)00268-0
1124 Jendrzejewski N., Trull T.W., Pineau F. and Javoy M., 1997. Carbon solubility in Mid-Ocean Ridge
1125 basaltic melt at low pressures (250-1950 bar). Chem. Geol. 138, 81-92.
1126 https://doi.org/10.1016/S0009-2541(96)00176-3
1127 Kamenetsky V.S. and Yaxley G.M., 2015. Carbonate-silicate liquid immiscibility in the mantle
1128 propels kimberlite magma ascent. Geochim. Cosmochim. Acta 158, 48-56.
1129 https://doi.org/10.1016/j.gca.2015.03.004
1130 Kawai N. and Endo S., 1970. The generation of ultrahigh hydrostatic pressures by a split sphere
1131 apparatus. Rev. of Sci. Instr. 41, 1178–1181. https://doi.org/10.1063/1.1684753

Kawamoto T. and Holloway J.R., 1997. Melting temperature and partial melt chemistry of H_2O-saturated mantle peridotite to 11 GPa. Science 276, 240-243. DOI:10.1126/science.276.5310.240

Khitarov N.I. and Kadik A.A., 1973. Water and carbon dioxide in magmatic melts and peculiarities of the melting process. Contrib. Mineral. Petrol. 41, 205-215. https://doi.org/10.1007/BF00371031

Kim E.J., Fei y. and Lee S.K., 2018. Effect of pressure on the short-range structure and speciation of carbon in alkali silicate and aluminosilicate glasses and melts at high pressure up to 8 GPa: ^{13}C, ^{27}Al, ^{17}O and ^{29}Si solid-state NMR study. Geochim. Cosmochim. Acta 224, 327-343. https://doi.org/10.1016/j.gca.2018.01.006

King P.L. and Holloway J.R., 2002. CO_2 solubility and speciation in intermediate (andesitic) melts: the role of H_2O and composition. Geochim. Cosmochim. Acta 66, 1627-1640. https://doi.org/10.1016/S0016-7037(01)00872-9

Kiseeva E.S., Yaxley G.M., Hermann J., Litasov K.D., Rosenthal A. and Kamenetsky V.S., 2012. An experimental study of carbonated eclogite at 3.5-5.5 GPa - Implications for silicate and carbonate metasomatism in the cratonic mantle. J. Petrol. 53, 727-759. DOI:10.1093/petrology/egr078

Konschak A. and Keppler A., 2014. The speciation of carbon dioxide in silicate melts. Contrib. Mineral. Petrol. 167, 998-1011. DOI:10.1007/s00410-014-0998-2

Kushiro I., Yoder H.S. and Nishikawa M., 1968. Effect of water on the melting of enstatite. GSA Bull. 79, 1685-1692. https://doi.org/10.1130/0016-7606(1968)79[1685:EOWOTM]2.0.CO;2

Labrosse S., Hernlund J. W. and Coltice N., 2007. A crystallizing dense magma ocean at the base of the Earth's mantle. Nature 450, 866–869. DOI:10.1038/nature06355

Lange R.A. and Carmichael I.S.E., 1987. Densities of Na_2O-K_2O-CaO-MgO-FeO-Fe_2O_3-Al_2O_3-TiO_2-SiO_2 liquids: new measurements and derived partial molecular properties. Geochim. Cosmochim. Acta 51, 2931-2946. https://doi.org/10.1016/0016-7037(87)90368-1

Lebrun T., Massol H., Chassefière E., Davaille A., Marcq E., Sarda P., Leblanc F. and Brandeis G., 2013. Thermal evolution of an early magma ocean in interaction with the atmosphere, J. Geophys. Res. Planets 118, 1–22. DOI:10.1002/jgre.20068

Le Losq C. and Neuville D.R., 2013. Effect of the Na/K mixing on the structure and the rheology of tectosilicate silica-rich melts. Chem. Geol. 346, 57–71. https://doi.org/10.1016/j.chemgeo.2012.09.009

Le Losq C., Neuville D.R., Moretti R. and Roux J., 2012. Determination of water content in silicate glasses using Raman spectrometry: Implications for the study of explosive volcanism. Am. Mineral 97, 779-790. https://doi.org/10.2138/am.2012.3831

Le Losq C., Neuville D.R., Florian P., Henderson G. S. and Massiot D., 2014. The role of Al^{3+} on rheology and structural changes in sodium silicate and aluminosilicate glasses and melts. Geochim. Cosmochim. Acta 126, 495-517. https://doi.org/10.1016/j.gca.2013.11.010

Le Losq C., Berry A.J., Kendrick M.A., Neuville D.R., H.St.C. O'Neill, 2019. Determination of the oxidation state of iron in Mid-Ocean Ridge basalt glasses by Raman spectroscopy. Am. Mineral 104, 1032-1042. https://doi.org/10.2138/am-2019-6887

1173 Le Losq, C., Cicconi, M.R., Greaves, G.N., Neuville, D.R., 2019. Silicate Glasses, in: Musgraves
1174 J.D., Hu J., Calvez L. (eds), Springer Handbook of Glass. Springer., Cham., pp. 441-503.
1175 https://doi.org/10.1007/978-3-319-93728-1_13
1176 Lenoir M., Grandjean A., Poissonnet S. and Neuville D.R., 2009. Quantitation of sulfate solubility in
1177 borosilicate glasses using Raman spectroscopy. J. Non-Crystal. Solids 355, 1468-1473.
1178 https://doi.org/10.1016/j.jnoncrysol.2009.05.015
1179 Lenoir M., Neuville D.R., Malki M., and Grandjean A., 2010. Volatilization kinetics of sulphur from
1180 borosilicate melts. A correlation between sulphur diffusion and melt viscosity. J. Non-Crystal.
1181 Solids 356, 2722-2727. DOI:10.1016/j.jnoncrysol.2010.09.077
1182 Lesne P., Scaillet B., Pichavant M. and Beny J.-M., 2011. The carbon dioxide solubility in alkali
1183 basalts: an experimental study. Contrib. Mineral. Petrol. 162, 153-168. DOI:10.1007/s00410-
1184 010-0585-0
1185 Li Y., Dasgupta R. and Tsuno K., 2017. Carbon contents in reduced basalts at graphite saturation:
1186 Implications for the degassing of Mars, Mercury, and the Moon. J. Geophys. Res. Planets 122,
1187 1300-1320. DOI:10.1002/2017JE005289
1188 Liu D., Zhu Y., Ding J., Lin X. and Fan X., 2015. Experimental investigation of carbon fiber
1189 reinforced poly(phenylene sulfide) composites prepared using a double-belt press. Composites
1190 Part B 77, 363-370. http://dx.doi.org/10.1016/j.compositesb.2015.03.062
1191 Long D.A., 1977. Raman Spectroscopy, pp. 292, McGraw-Hill, New York.
1192 Magnien V., Neuville D.R., Cormier L., Roux J., Hazemann J.-L., Pinet O. and Richet P., 2006.
1193 Kinetics of iron redox reactions in silicate liquids: A high-temperature X-ray absorption and
1194 Raman spectroscopy study. J. Nucl. Mat. 352, 190–195. DOI:10.1016/j.jnucmat.2006.02.053
1195 Magnien V., Neuville D.R., Cormier L., Roux J., Hazemann J.-L., Manara D., Grandjean A., Pinet O.,
1196 de Ligny D., Pascarelli S., Vickridge I., Pinet O., Richet P., 2008. Kinetics and mechanisms of
1197 iron redox reactions in silicate melts: The effects of temperature and alkali cations. Geochim.
1198 Cosmochim. Acta 72, 2157-2168. DOI:10.1016/j.gca.2008.02.007
1199 Manara D., Grandjean A., Pinet O., Dussossoy J.L. and Neuville D.R., 2007. Sulphur behavior in
1200 silicate glasses and melts: implications for sulfate incorporation in nuclear waste glasses as a
1201 function of alkali cation and V_2O_5 content. J. Non-Crystal. Solids 353, 12–23.
1202 https://doi.org/10.1016/j.jnoncrysol.2006.09.041
1203 Marty B., 2012. The origins and concentrations of water, carbon, nitrogen and noble gases on
1204 Earth, Earth Planet. Sci. Lett. 313–314, 56–66. DOI:10.1016/j.epsl.2011.10.040
1205 Mattey D.P., 1991. Carbon dioxide solubility and carbon isotope fractionation in basaltic melt.
1206 Geochim. Cosmochim. Acta 55, 3467-3473. https://doi.org/10.1016/0016-7037(91)90508-3
1207 McMillan P. F., 1984. Structural studies of silicate glasses and melts – applications and limitations
1208 of Raman spectroscopy. Am. Mineral. 69, 622–644.
1209 McMillan P.F. and Remmele R.L. Jr., 1986. Hydroxyl sites in SiO_2 glass: A note on infrared and
1210 Raman spectra. Am. Mineral. 71, 772–778.
1211 Mercier M., Muro A.D., Métrich, N., Giordano D., Belhadj O. and Mandeville C.W., 2010.
1212 Spectroscopic analysis (FTIR, Raman) of water in mafic and intermediate glasses and glass
1213 inclusions. Geochim. Cosmochim. Acta 74(19), 5641-5656. DOI:10.1016/j.gca.2010.06.020
1214 Mitchell R.H., 2008. Petrology of hypabyssal kimberlites: Relevance to primary magma
1215 compositions. J. Volcanol. Geotherm. Res. 174, 1–8. DOI:10.1016/j.jvolgeores.2007.12.024

Morizet Y., Brooker R. A. and Kohn S. C., 2002. CO_2 in haplophonolite melt: solubility, speciation and carbonate complexation. Geochim. Cosmochim. Acta 66, 1809–1820. https://doi.org/10.1016/S0016-7037(01)00893-6

Morizet Y., Brooker R.A., Iacono-Marziano G. and Kjarsgaard B.A., 2013. Quantification of dissolved CO_2 in silicate glasses using micro-Raman spectroscopy. Am. Mineral. 98, 1788-1802. https://doi.org/10.2138/am.2013.4516

Morizet Y., Paris M., Gaillard F. and Scaillet B., 2014. Carbon dioxide in silica-undersaturated melt. Part I: The effect of mixed alkalis (K and Na) on CO_2 solubility and speciation. Geochim. Cosmochim. Acta 141, 45–61. http://dx.doi.org/10.1016/j.gca.2014.06.014

Morizet Y., Paris M., Sifré D., Di Carlo I. and Gaillard F., 2017. The effect of Mg concentration in silicate glasses on CO2 solubility and solution mechanism: Implication for natural magmatic systems. Geochim. Cosmochim. Acta 198, 115-130. http://dx.doi.org/10.1016/j.gca.2016.11.006

Morizet Y., Larre C., Di Carlo I. and Gaillard F., 2020. High S and high CO_2 contents in haplokimberlite: An experimental and Raman spectroscopic study. Mineral. Petrol. 114, 363–373. https://doi.org/10.1007/s00710-020-00711-1

Moore J.G., Batchelder J.N. and Cunningham C.G., 1977. CO_2-filled vesicles in mid-ocean basalt. J. Volcanol. Geotherm. Res. 2, 309-327. https://doi.org/10.1016/0377-0273(77)90018-X

Mourão C., Moreira M., Mata J., Raquin A. and Madeira J., 2012. Primary and secondary process constraining the noble gas isotopic signatures of carbonatites and silicate rocks from Brava Island: evidence for a lower mantle origin of the Cape Verde plume. Contrib. Mineral. Petrol. 163, 995-1009. DOI:10.1007/s00410-011-0711-7

Mysen B.O., 1976. The role of volatiles in silicate melts: solubility of carbon dioxide and water in feldspar, pyroxene, and feldspathoïd melts to 30 kbar and 1625°C. Am. J. Sci. 276, 969-996. DOI:10.2475/ajs.276.8.969

Mysen B.O., 1990. Effect of pressure, temperature, and bulk composition on the structure and species distribution in depolymerized alkali aluminosilicate melts and quenched melts. J. Geophys. Res. 95, 148-227. https://doi.org/10.1029/JB095iB10p15733

Mysen B.O. and Virgo D., 1980. Solubility mechanisms of carbon dioxide in silicate melts: a Raman spectroscopic study. Am. Mineral. 65, 885-899.

Mysen B.O., Virgo D., Wendy J.H. and Scarfe C.M., 1980. Solubility mechanisms of H_2O in silicate melts at high pressures and temperatures: a Raman spectroscopic study. Am. Mineral. 65, 900–914.

Mysen B.O., Finger L.W., Virgo D. and Seifert F.A., 1982. Curve-fitting of Raman spectra of silicate glasses. Am. Mineral. 67, 686–695.

Mysen B.O. and Virgo D., 1986. Volatiles in silicate melts at high pressure and temperature: 1. Interaction between OH groups and Si^{4+}, Al^{3+}, Ca^{2+}, Na^{+} and H^{+}. Chem. Geol. 57, 303–331. https://doi.org/10.1016/0009-2541(86)90056-2

Nakano S., Moritoki M. and Ohgaki K., 1998. High-pressure phase equilibrium and Raman microprobe spectroscopic studies on the CO_2 hydrate system. J. Chem. Eng. Data 43, 807-810. https://doi.org/10.1021/je9800555

Neuville D.R., 2006. Viscosity, structure and mixing in (Ca, Na) silicate melts. Chem. Geol. 229, 28-41. DOI:10.1016/j.chemgeo.2006.01.008

Neuville D.R., Cormier L., Montouillout V., Florian P., Millot F., Rifflet J.-C. and Massiot D., 2008. Structure of Mg- and Mg/Ca aluminosilicate glasses: ^{27}Al NMR and Raman spectroscopy investigations. Am. Mineral. 93, 1721–1731. DOI: 10.2138/am.2008.2867

Neuville D.R., De Ligny D. and Henderson G. S., 2014. Advances in Raman spectroscopy applied to Earth and material sciences. Rev. Mineral. Geochem. 78, 509-541. https://doi.org/10.2138/rmg.2013.78.13

Ni H. and Keppler H., 2013. Carbon in Silicate Melts. Rev. Mineral. Geochem. 75, 251-287. DOI: 10.2138/rmg.2013.75.9

Nowak M., Schreen D. and Spickenbom K., 2004. Argon and CO_2 on the race track in silicate melts: A tool for the development of a CO_2 speciation and diffusion model. Geochim. Cosmochim. Acta 68, 5127-5138. DOI:10.1016/j.gca.2004.06.002

Okumura S. and Hirano N., 2013. Carbon dioxide emission to Earth's surface by deep-sea volcanism. Geology 41, 1167-1170. https://doi.org/10.1130/G34620.1

Pan V., Holloway J.R. and Hervig R.L., 1991. The pressure and temperature dependence of carbon dioxide solubility in tholeiitic basalt melts. Geochim. Cosmochim. Acta 55, 1587-1595. https://doi.org/10.1016/0016-7037(91)90130-W

Papale P., 1999. Modeling of the solubility of a two-component H_2O + CO_2 fluid in silicate liquids. Am. Min. 84, 477-492. doi.org/10.2138/am-1999-0402

Papale P., Moretti R. and Barbato D., 2006. The compositional dependence of the saturation surface of H_2O+CO_2 fluids in silicate melts. Chemical Geology 229, 78–95. https://doi.org/10.1016/j.chemgeo.2006.01.013

Pawley A.R., Holloway J.R and McMillan P.F., 1992. The effect of oxygen fugacity on the solubility of carbon-oxygen fluids in basaltic melt. Earth Planet. Sci. Lett. 110, 213-225. https://doi.org/10.1016/0012-821X(92)90049-2

Pineau F., Shilobreeva S., Hekinian R., Bideau D. and Javoy M., 2004. Deep-sea explosive activity on the Mid-Atlantic Ridge near 34°50'N: a stable isotope (C, H, O) study. Chem. Geol. 211, 159-175. DOI:10.1016/j.chemgeo.2004.06.029

Poirier J-P., 1994. Light elements in the Earth's outer core: A critical review. Phys. Earth Planet. Int. 85, 319-337. https://doi.org/10.1016/0031-9201(94)90120-1

Pommier A., Grove T.L. and Charlier B., 2012. Water storage and early hydrous melting of the Martian mantle. Earth Planet. Sci. Lett. 333-334, 272-281. https://doi.org/10.1016/ j.epsl.2012.03.030

Poole J.P., 1949. Low-temperature viscosity of alkali silicate glasses. J. Am. Ceram. Soc. 32, 230-233. https://doi.org/10.1111/j.1151-2916.1949.tb18952.x

Rai C.S., Sharma S.K., Muenow D.W., Matson D.W. and Byers C.D., 1983. Temperature dependence of CO_2 solubility in high pressure quenched glasses of diopside composition. Geochim. Cosmochim. Acta 47, 953-958. https://doi.org/10.1016/0016-7037(83)90161-8

Richet P., Lejeune A.-M., Holtz F. and Roux J., 1996. Water and the viscosity of andesite melts, Chem. Geol. 128, 185-197. https://doi.org/10.1016/0009-2541(95)00172-7

Roskosz M., Mysen B.O. and Cody G.D., 2006. Dual speciation of nitrogen in silicate melts at high pressure and temperature: An experimental study. Geochim. Cosmochim. Acta 70, 2902–2918. DOI:10.1016/j.gca.2006.03.001

1300 Roskosz M., Toplis M.J., Neuville D.R. and Mysen B.O., 2008. Quantification of the kinetics of iron
1301 oxidation in silicate melts using Raman spectroscopy and assessment of the role of oxygen
1302 diffusion. Am. Mineral. 93, 1749-1759. DOI:10.2138/am.2008.2861
1303 Russel J.K., Porritt L.A., Lavallée I. and D.B. Dingwell, 2012. Kimberlite ascent by assimilation-
1304 fueled buoyancy. Nature 481, 352-356. https://doi.org/10.1038/nature10740
1305 San Miguel A. and Toulemonde P., 2005. High-pressure properties of group IV clathrates, High
1306 Pressure Res. 25, 159-185. DOI:10.1080/08957950500319464
1307 Sarda P. and Graham D., 1990. Mid-ocean ridge popping rocks and outgassing processes at ridge
1308 crests, Earth Planet. Sci. Lett. 97, 268-289. https://doi.org/10.1016/0012-821X(90)90047-2
1309 Sarda P. and Guillot B., 2005. Breaking of Henry's law for noble gas and CO_2 solubility in silicate
1310 melt under pressure. Nature 436, 95-98. DOI:10.1038/nature03636
1311 Sarda P., Staudacher Th. and Allègre C.J., 1985. $^{40}Ar/^{36}Ar$ in MORB glasses: constraints on
1312 atmosphere and mantle evolution, Earth Planet. Sci. Lett. 72, 357-375.
1313 https://doi.org/10.1016/0012-821X(85)90058-5
1314 Sarda P., Chamorro E., Neuville D., Sator N., Guillot B. and San Miguel A., 2009. Raman
1315 determination of C concentration in silicate melt under pressure: carbon solubility in MORB and
1316 mantle melting scenario, Geophysical Res. Abstracts 11, EGU2009-9394, EGU General
1317 Assembly, Vienna.
1318 Schmidt B. and Keppler H., 2002. Experimental evidence for high noble gas solubilities in silicate
1319 melts under mantle pressures. Earth Planet Sci. Lett. 195, 277-290.
1320 https://doi.org/10.1016/S0012-821X(01)00584-2
1321 Schramm C.M., de Jong B.H.W.S., Parziale V.E., 1984. ^{29}Si Magic Angle Spinning NMR study on
1322 local silicon environments in amorphous and crystalline lithium silicates. J. Am. Chem. Soc. 106,
1323 4396-4402. https://doi.org/10.1021/ja00328a018
1324 Scott E.R.D., 1971. New carbide, $(Fe,Ni)_{23}C_6$, found in iron meteorites. Nature Phys. Sci. 229, 61-
1325 62. https://doi.org/10.1038/physci229061a0
1326 Sharma S.K., 1979. Structure and solubility of carbon dioxide in silicate glasses of diopside and
1327 sodium melilite compositions at high pressures from Raman spectroscopic data. Carn. Inst.
1328 Washington Yearb. 78, 532-537.
1329 Shatskiy A., Gavryushkin P.N., Sharygin I.S., Litasov K.D., Kupriyanov I.N., Higo Y., Borzdov Y.M.,
1330 Funakoshi K.-I., Palyanov Y.N. and Ohtani E., 2013. Melting and subsolidus phase relations in
1331 the system Na_2CO_3-$MgCO_3 \pm H_2O$ at 6 GPa and the stability of $Na_2Mg(CO_3)_2$ in the upper mantle.
1332 Am. Mineral. 98, 2172-2182. DOI:10.2138/am.2013.4418
1333 Shishkina T.A., Botcharnikov R.E., Holtz F., Almeev R.R. and Portnyagin M.V., 2010. Solubility of
1334 H_2O- and CO_2-bearing fluids in tholeiitic basalts at pressures up to 500 MPa, Chem. Geol. 277,
1335 115-125. doi:10.1016/j.chemgeo.2010.07.014
1336 Schminke H.U., Robinson P.T., Ohnmacht W. and Flower M.F.J., 1978. Basaltic hyaloclastites from
1337 hole 396B, DSDP LEG 46. In: Dmitriev L., Heirtzler et al., 1978. Initial Reports of the Deep-Sea
1338 Drilling Project 46: Washington (US Government Printing Office), p. 341-348.
1339 DOI:10.2973/dsdp.proc.46.122.1979
1340 Smith T.L. and Batiza R., 1989. New field and laboratory evidence for the origin hyaloclastite flows
1341 on seamount summits. Bull. Volcanol. 51, 96-114. https://doi.org/10.1007/BF01081979

1342 Shuker R. and Gammon R., 1970. Raman-scattering selection-rule breaking and the density of
1343 states in amorphous materials. Phys. Rev. Lett. 25(4), 222-225.
1344 https://doi.org/10.1103/PhysRevLett.25.222
1345 Sohn R.A. et al., 2008. Explosive volcanism on the ultraslow-spreading Gakkel ridge, Artic Ocean.
1346 Nature 453, 1236-1238. DOI:10.1038/nature07075
1347 Solomatova N.V., Caracas R. and Manning C.E., 2019. Carbon sequestration during core formation
1348 implied by complex carbon polymerization. Nature Communications 10, 1-7.
1349 https://doi.org/10.1038/s41467-019-08742-9.
1350 Sparks R.S.J., Baker L., Brown R.J., Field M., Schumacher J., Stripp G. and Walters A., 2006.
1351 Dynamical constraints on kimberlite volcanism. J. Volcanol. Geotherm. Res. 155, 18-48.
1352 DOI:10.1016/j.jvolgeores.2006.02.010
1353 Spivak A.V., Litvin Yu. A., Ovsyannikov S.V., Dubrovinskaia N.A. and Dubrovinsky L.S., 2012.
1354 Stability and breakdown of $Ca^{13}CO_3$ melt associated with formation
1355 of ^{13}C-diamond in static high pressure experiments up to 43 GPa and 3900 K. J. Solid State
1356 Chem. 191, 102-106. DOI:10.1016/j.jssc.2012.02.041
1357 Stanley B.D., Hirschmann M.M. and Withers A.C, 2011. CO_2 solubility in Martian basalts and
1358 Martian atmospheric evolution. Geochim. Cosmochim. Acta 75, 5987–6003.
1359 DOI:10.1016/j.gca.2011.07.027
1360 Stanley B.D., Schaub D.R. and Hirschmann M.M., 2012. CO_2 solubility in primitive Martian basalts
1361 similar to Yamato 980459, the effect of composition on CO_2 solubility of basalts, and the
1362 evolution of the Martian atmosphere. Am. Mineral. 97, 1841-1848.
1363 https://doi.org/10.2138/am.2012.4141
1364 Stolen R.H. and Walrafen G.E., 1976. Water and its relation to broken bond defects in fused silica.
1365 J. Chem. Phys. 64(6), 2623-2631. https://doi.org/10.1063/1.432516
1366 Stolper E. and Holloway J.R., 1988. Experimental determination of carbon dioxide in molten basalt
1367 at low-pressure. Earth Planet. Sci. Lett. 87, 397-408. https://doi.org/10.1016/0012-
1368 821X(88)90004-0
1369 Suito K., Namba J., Horikawa T., Taniguchi Y., Sakurai N., Kobayashi M., Onodera A., Shimomura
1370 O. and Kikegawa T., 2001. Phase relations of $CaCO_3$ at high pressure and high temperature.
1371 Am. Mineral. 86, 997-1002.
1372 Thomas R., 2000. Determination of water concentrations of granite melt-inclusion by confocal laser
1373 Raman microprobe spectroscopy. Am. Mineral. 85, 868–872.
1374 Toulemonde P., Adessi Ch., Blase X., San Miguel, A. and Tholence J.L., 2005. Superconductivity in
1375 the $(Ba_{1-x}Sr_x)_8Si_{46}$ clathrates ($x \leq 0.75$): Experimental and ab initio investigation. Phys. Rev. B
1376 71, 094504, 1-6. https://doi.org/10.1103/PhysRevB.71.094504
1377 Verweij H., Van den Boom H. and Breemer, R.E., 1977. Raman scattering of carbonate ions
1378 dissolved in potassium silicate glasses. J. Am. Ceram. Soc. 60, 529-34.
1379 https://doi.org/10.1111/j.1151-2916.1977.tb14099.x
1380 Vetere F., Behrens H., Holtz F. and Neuville D.R., 2006. Viscosity of andesitic melts—new
1381 experimental data and a revised calculation model. Chem. Geol. 228, 233-245.
1382 DOI:10.1016/j.chemgeo.2005.10.009
1383 Vinnik L., Breger L. and Romanowicz B., 1998. Anisotropic structures at the base of the Earth's
1384 mantle, Nature 393, 564-567. DOI:10.1038/31208

Virgo D., Mysen B.O. and Kushiro I., 1980. Anionic constitution of 1-atmosphere silicate melts: implications for the structure of igneous melts. Science 208, 1371-1373. DOI:10.1126/science.208.4450.1371

Vuilleumier R., Seitsonen A.P., Sator N. and Guillot B., 2015. Carbon dioxide in silicate melts at upper mantle conditions: Insights from atomistic simulations, Chem. Geol. 418, 77-88. http://dx.doi.org/10.1016/j.chemgeo.2015.02.027

Walker D., Carpenter M.A. and Hitch C.M., 1990. Some simplifications to multi-anvil devices for high pressure experiments. Am. Mineral. 75, 1020–1028.

Walrafen G.E., 1975. Raman spectra from Si–OH groups in solid optical fibers. J. Chem. Phys. 62(1), 297-298. https://doi.org/10.1063/1.430224

Walrafen G.E. and Samanta S.R., 1978. Infrared absorbance spectra and interactions involving OH groups in fused silica. J. Chem. Phys. 69(1), 493–495. https://doi.org/10.1063/1.436379

Whittington A., Richet P. and Holtz F., 2000. Water and the viscosity of depolymerized aluminosilicate melts. Geochim. Cosmochim. Acta 64, 3725-3736. https://doi.org/10.1016/S0016-7037(00)00448-8

Williams Q.and Garnero E., 1996. Seismic evidence for partial melt at the base of Earth's mantle. Science 273, 1528–1530. DOI: 10.1126/science.273.5281.1528

Woltring H.J., 1986. A Fortran package for generalized, cross-validatory spline smoothing and differentiation. Adv. Eng. Software 8(2), 104-113. https://doi.org/10.1016/0141-1195(86)90098-7

Wood B.J., 1993. Carbon in the core. Earth Plan et Sci. Lett. 117, 593-607.

Woolley A.R. and Church A.A., 2005. Extrusive carbonatites: A brief review. Lithos 85, 1-14. https://doi.org/10.1016/j.lithos.2005.03.018

Yaxley G.M. and Brey G.P., 2004. Phase relations of carbonate-bearing eclogite assemblages from 2.5 to 5.5 GPa: implications for petrogenesis of carbonatites. Contrib. Mineral. Petrol. 146, 606-619. DOI:10.1007/s00410-003-0517-3

Table 1

Starting compositions in wt.%; numbers in parentheses stand for CO_2-free composition, other numbers represent the complete composition, including added CO_2. Note that, for the samples in the 2nd column, the added carbonate was not weighted. The natural MORB is from the South Atlantic Ocean, labeled EW9309 14D-4g (Douglass et al., 1999), and its composition was kindly communicated by Jean-Guy Shilling.

Sample type	MORB (natural)	MORB (synthetic)		Haplo-basalts		Haplo-andesite	
Sample name	BPhE2, BPhE3	BPhE10, BPhE11, BPhE12		1010, 1011		1090	
SiO_2	(50.81)	50.40	(56.49)	41.66	(49.22)	54.93	(62.70)
TiO_2	(1.59)	1.63	(1.83)	0	0	0	0
Al_2O_3	(15.04)	14.93	(16.73)	20.20	(14.06)	20.85	(20.60)
FeO	(9.68)	0	0	0	0	0	0
MnO	(0.14)	0	0	0	0	0	0
MgO	(8.33)	8.26	(9.26)	11.98	(21.09)	3.39	(3.14)
CaO	(11.27)	11.18	(12.53)	9.87	(12.50)	8.10	(9.17)
Na_2O	(2.83)	2.82	(3.16)	2.73	(3.13)	4.34	(3.73)
K_2O	(0.28)	0	0	0	0	0	0
P_2O_5	(0.16)	0	0	0	0	0	0
Total silicate	(100)		(100)		(100)		(100)
CO_2 (added)	> 10	10.78		13.56		9.00	
Total with CO_2	-	100		100		100	

Table 2

Listed are experimental run conditions (P,T), major element microprobe analyzes of *vitreous* regions in quenched samples (wt.%), and CO_2 contents, as well as H_2O where measured, both obtained by Raman spectroscopy (wt.%). Typical 1σ errors on temperature are ~50°C for BPhE samples (due to an important extrapolation for Belt press experiments) and 25°C for the other samples (temperature is measured in multi-anvil press experiments). Knowledge of pressure is precise to about 5% (1σ) for the Belt press, and about 0.25 GPa (1σ) for the multi-anvil press.

Electron microprobe conditions are the following: for BPhE samples, Clermont-Ferrand, Cameca SX100: acceleration tension: 15 kV, beam current: 8 nA, spot size: 20 micrometers, counting time: 10 s on peak. For 1010, 1011 and 1090, Camparis, Cameca SX100: 30 kV, 30 nA, 5 s on peak.

Results for CO_2 rely on the calibration shown in Fig. 2 and correspond to the average concentration for each sample. Those samples used to establish the calibration are those for which H_2O was measured (with the method of Le Losq et al., 2012) and these H_2O results are reported here. Analytical uncertainties at 1σ are typically 1% for major elements and are reported here for CO_2 and H_2O. Notice that, for samples 1011 and 1090, the major element data is likely perturbated by sample non-homogeneity. *u.s.* : undersaturated.

Sample	BPhE2	BPhE3	BPhE10	BPhE11	BPhE12	1010	1011	1090
P(GPa)	2	3	2	4	1.5	5	8.5	5
1 σ P	0.1	0.15	0.1	0.2	0.08	0,25	0,25	0,25
T(K)	1920	2003	1920	2128	1824	1873	1873	1873
1 σ T	48	54	48	65	41	25	25	25
SiO_2	48.87	47.52	54.38	53.57	53.89	42.90	55.57	67.29
TiO_2	1.56	1.46	1.65	1.68	1.75	0.05	0.03	0.03
Al_2O_3	15.45	15.00	17.01	16.33	17.02	20.05	19.09	26.63
FeO	5.29	2.29	0.01	0.02	0.01	0.02	0.02	0.04
MnO	0.17	0.16	0.01	0.01	0.02	0.02	0.01	0.01
MgO	7.77	7.40	7.81	7.41	7.58	15.94	8.07	4.56
CaO	13.81	16.13	11.85	11.40	11.82	11.46	8.68	0.49
Na_2O	2.47	2.31	2.77	2.60	2.81	3.46	8.19	0.44
K_2O	0.29	0.30	0.03	0.06	0.04	0.13	0.27	0.03
P_2O_5	0.15	0.17	0.06	0.04	0.07	0	0	0
SrO	0	0	0	0	0	0.02	0.06	0.03
GeO_2	0	0	0	0	0	0.02	0.04	0.08
Total	95.89	92.74	95.58	93.14	95.02	93.34	100.02	99.62
CO_2^{Raman}	2.65	4.21	1.56	4.67	1.78	5.97	>13.6 (*u.s.)*	8.5
1 σ CO_2	0.28	0.25	0.80	0.47	0.19	0.53	-	0.85
H_2O	1,24	2,55	2,25	n.m.	2,62	0,54	-	-

1 σ H_2O	0,02	0,43	0,74	-	0,26	0,17	-	-
sum	99.77	99.49	99.38	> 97.81	99.50	99.84	-	-

1452

1453

1454

1455

Figure captions

Figure 1a: Raman spectra of a basalt glass, from top to bottom (i) uncorrected, (ii) after the Long correction, and (iii) baseline-corrected and normalized. Note the baseline shown in the second spectrum. a.u.: arbitrary units. Bands in the 20-1200 cm^{-1} portion of the spectra are assigned to vibrations of the SiO_4 and AlO_4 tetrahedral network of the basalt glass (see the review of Neuville et al., 2014, and references therein), the peak at ~1085 cm^{-1} and the doublet at ~1400-1600 cm^{-1} are respectively assigned to the symmetric and asymmetric stretching mode of the CO_3^{2-} groups (Verweij et al., 1977; Mysen and Virgo, 1980; Rai et al., 1983; Brooker et al., 1999), and the band extending between 3000 and 4000 cm^{-1} is assigned to O-H stretching in H_2O_{mol} and OH^- groups (Walrafen, 1975; Stolen and Walrafen, 1976; Walrafen et Samanta, 1978; Mysen et al., 1980, Mysen and Virgo, 1986; McMillan and Remmele, 1986).

Figure 1b: Examples of deconvolution on Raman spectra in the region 800 - 1200 cm^{-1}, which includes the several peaks of the Q^n tetrahedral species (n = 0 to 4) and the peak due to the C-O symmetric stretching of CO_3^{2-} located at 1070-1090 cm^{-1} in basaltic compositions and 1046 cm^{-1} in KS samples. Spectra A and B were taken from basaltic sample BPhE11, C and D from KS samples, where D is the KS with 3.6 wt.% CO_2 that is used in the calibration shown in Fig. 2.

Figure 2: Calibration of the Raman method of CO_2 measurement in silicate material. Area of the ~1085 cm^{-1} CO_2 Raman peak vs. CO_2 concentration. Shown are our potassium silicate (KS) samples, our natural MORB samples with added carbonate (BPh) and our artificial basaltic sample, 1010). For BPhE and 1010 samples, CO_2 concentrations were determined by difference to 100% of the sum of the major elements obtained by electron microprobe analysis and H_2O by Raman spectroscopy. The best straight line passing through these points has a slope of 0.063453±0.002156 (correlation coefficient of 0.966), identical within error to that determined by Morizet et al., 2013).

Figure 3: a) Polished section of sample BPhE2, a natural basalt loaded with calcium carbonate and exposed to 2 GPa, showing the occurrence of a bubble at the top of the capsule after quench, while the carbonate powder was loaded at the bottom of the capsule. This bubble suggests this sample is saturated in CO_2. The height of the capsule is 2.5 mm.
b) Raman map of basaltic sample 1010 (5 GPa) showing CO_2 concentrations in wt.%. Note the bubble in the right-hand side bottom corner of the picture, highlighted by a dashed line, and the variations of CO_2 increasing toward the bubble. The top of the capsule, when at high pressure, was on the right side.

Figure 4: Raman mapping, with CO_2 concentrations reported in wt.%, of a) basaltic sample BPhE10, 2 GPa) with 19 measurement spots, showing the strong CO_2 heterogeneity of this sample, where a bubble is probably located inside the platinum at the top of the capsule or was lost in the experiment, and b) sample BPhE3 (3 GPa), showing the relative CO_2 homogeneity of this sample, a variability of about 0.2 % for the 4 spots shown (6 spots are available). Note that the global CO_2

concentration obtained for BPhE10 is very different from the lowest and the highest values, but identical to that reported by Mattey (1991) for a similar composition and the same pressure, pointing to the interest to realize such a sample mapping.

Figure 5: Raman mapping of a 30 μm x 30 μm area of sample 1090. The probed depth was ~2μm and the spot of the laser beam ~1-2 μm^2. On the left are shown a Raman spectrum from one of the aragonite crystals, a spectrum from the glass alone, and a spectrum from the aragonite-glass mixture (with the ~1080 cm^{-1} peak shown in green). The color-scale represents the intensity of the ~1080 cm^{-1} CO_3^{2-} stretch peak from aragonite microcrystals in the glass normalized to the maximum intensity found in the aragonite crystal at the bottom left-hand side of the map. We assume, here, that this normalized intensity of the crystalline CO_3^{2-} peak depends linearly on the fraction of nano- and micro-crystals present in the glass.

Figure 6: photograph of a section of sample 1011 (8.5 GPa) in reflected light. The circle shows where the Raman spectrum shown in Fig. 7 was taken.

Figure 7: From top down are displayed Raman spectra taken in sample 1011 for one glass region and one silicate crystal, then the reference Raman spectrum for the silicate mineral pyrope, a garnet, the spectrum of carbonate mineral eitelite, $Na_2Mg(CO_3)_2$, and the spectrum of aragonite. The thin peaks generated by eitelite microcrystals are visible in the spectrum of glass.

Figure 8: CO_2 concentration (weight ratio) in various mafic melts plotted as a function of total pressure in GPa, with 1-σ experimental errors. Shown are the experimental data generated in this work, as well as several curves obtained by molecular dynamics simulations for similar compositions (name of composition and temperatures indicated). Sample BPhE2 was omitted since it has a too small number of measurements (see text). These data correspond to melts saturated with CO_2, thus solubility, except for the triangle with an arrow showing that the true value for sample 1011 is higher because this sample was clearly under-saturated at 8.5 GPa. Also shown are, using open symbols, some experimental results for similar compositions in the range 0 – 2.5 GPa published previously by Pan et al. (1991), Mattey (1991) and Stanley et al. (2011). Other data in the pressure range between 0 and 0.5 GPa are impossible to show at this scale, including Stolper and Holloway (1988), Pawley et al. (1992), Dixon et al. (1995), Jendrzejewski et al. (1997), Botcharnikov et al. (2005), Shishkina et al. (2010) and others, but are consistent with each other. The empty circle at 6 GPa is from Kim et al (2018) for albite melt. The dashed-dotted straight line is an extrapolation of the Henry's law proposed by Dixon et al. (1995) based on the shown data of Pan et al. (1991) and Mattey (1991). The dashed-dotted curves labeled 'Eguchi & Dasgupta 2018' are from the thermodynamic model of Eguchi and Dasgupta (2018) where the higher curve is for a composition of MORB and the lower curve for a haplo-basalt. A zoom on the low-pressure region of this figure is presented in the supplement (Fig. S7).

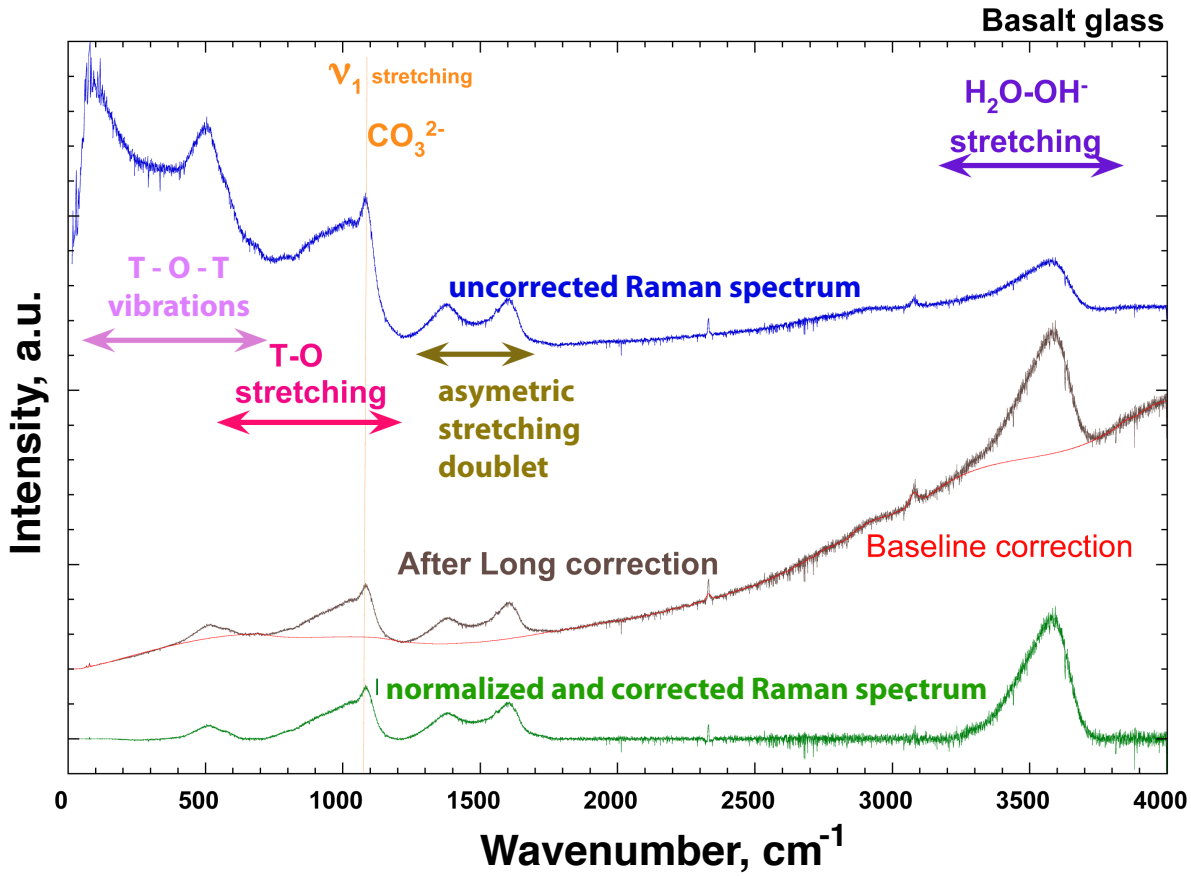
Basalt glass
ν1 stretching
CO3 2-
H2O-OH-
stretching
T - O - T
vibrations
uncorrected Raman spectrum
T-O
stretching
asymetric
stretching
doublet
After Long correction
Baseline correction
normalized and corrected Raman spectrum
Intensity, a.u.
0
500
1000
1500
2000
2500
3000
3500
4000
Wavenumber, cm-1

Figure 1a

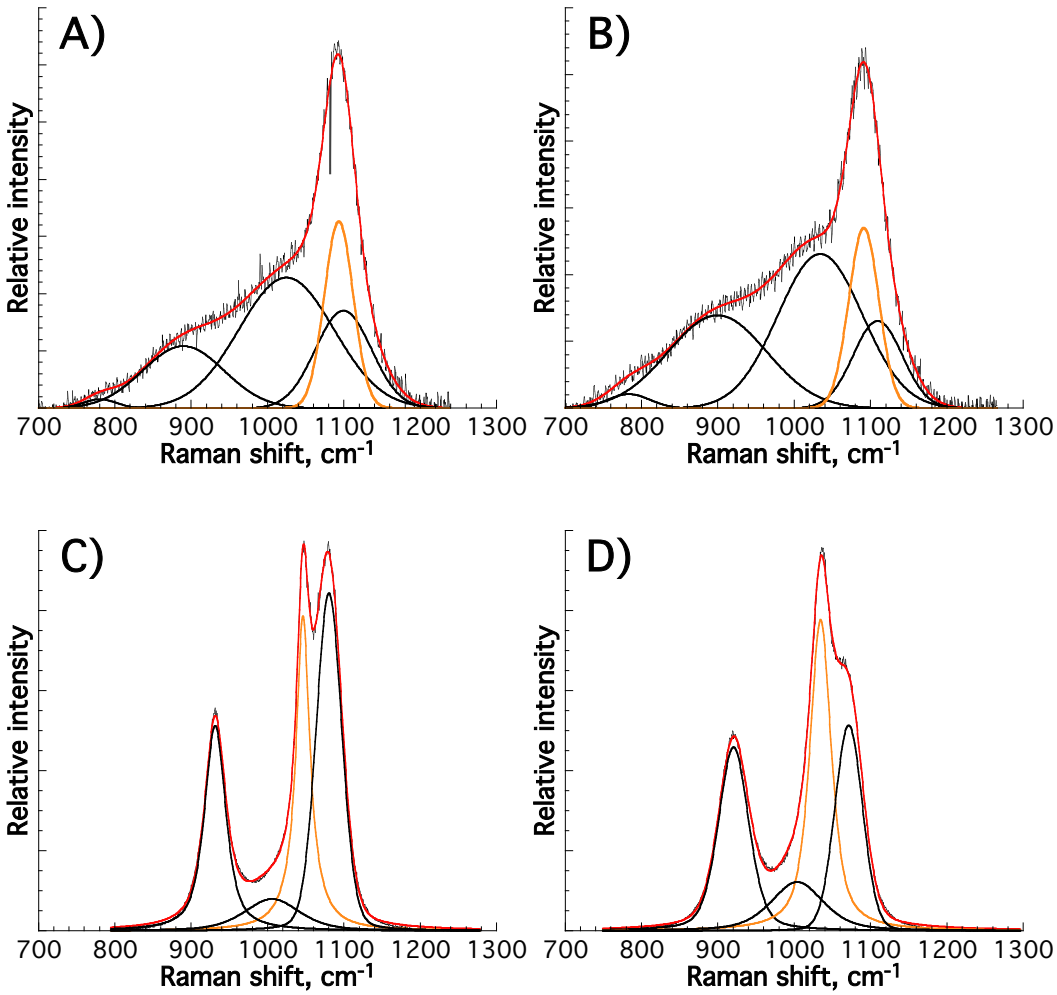
A)
B)
C)
D)
Relative intensity
Raman shift, cm-1
700
800
900
1000
1100
1200
1300

Figure 1b

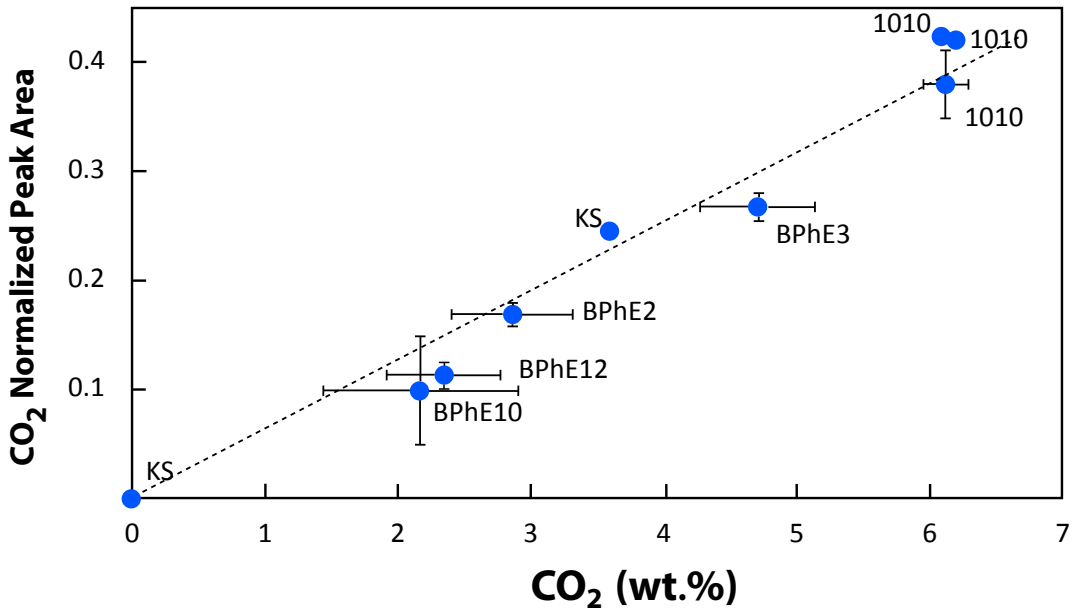
1010
1010
1010
KS
BPhE3
BPhE2
BPhE12
BPhE10
KS
0.4
0.3
0.2
0.1
0
1
2
3
4
5
6
7
CO2 Normalized Peak Area
CO2 (wt.%)

Figure 2

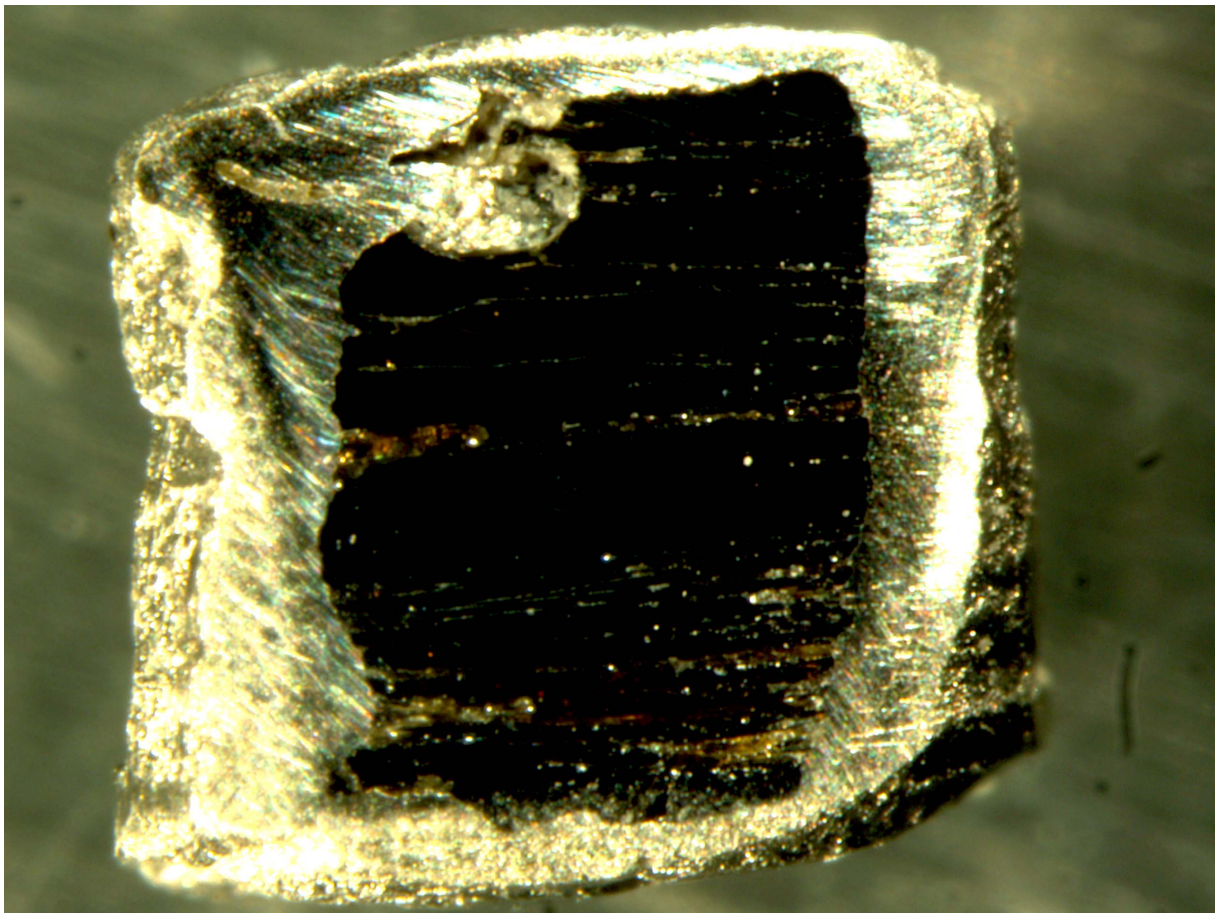

Figure 3a

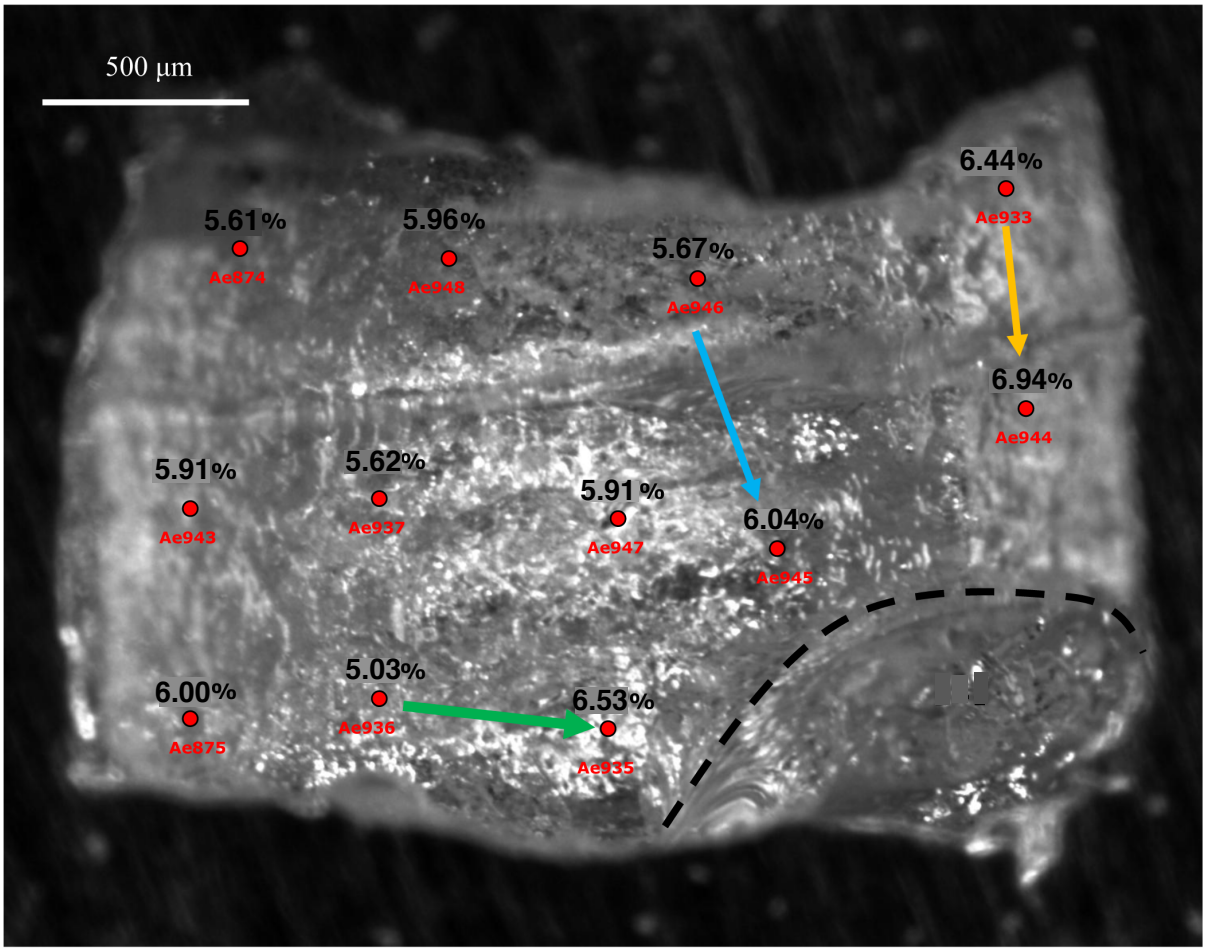
500 µm
5.61%
Ae874
5.96%
Ae948
5.67%
Ae946
6.44%
Ae933
6.94%
Ae944
5.91%
Ae943
5.62%
Ae937
5.91%
Ae947
6.04%
Ae945
6.00%
Ae875
5.03%
Ae936
6.53%
Ae935

Figure 3b

1646

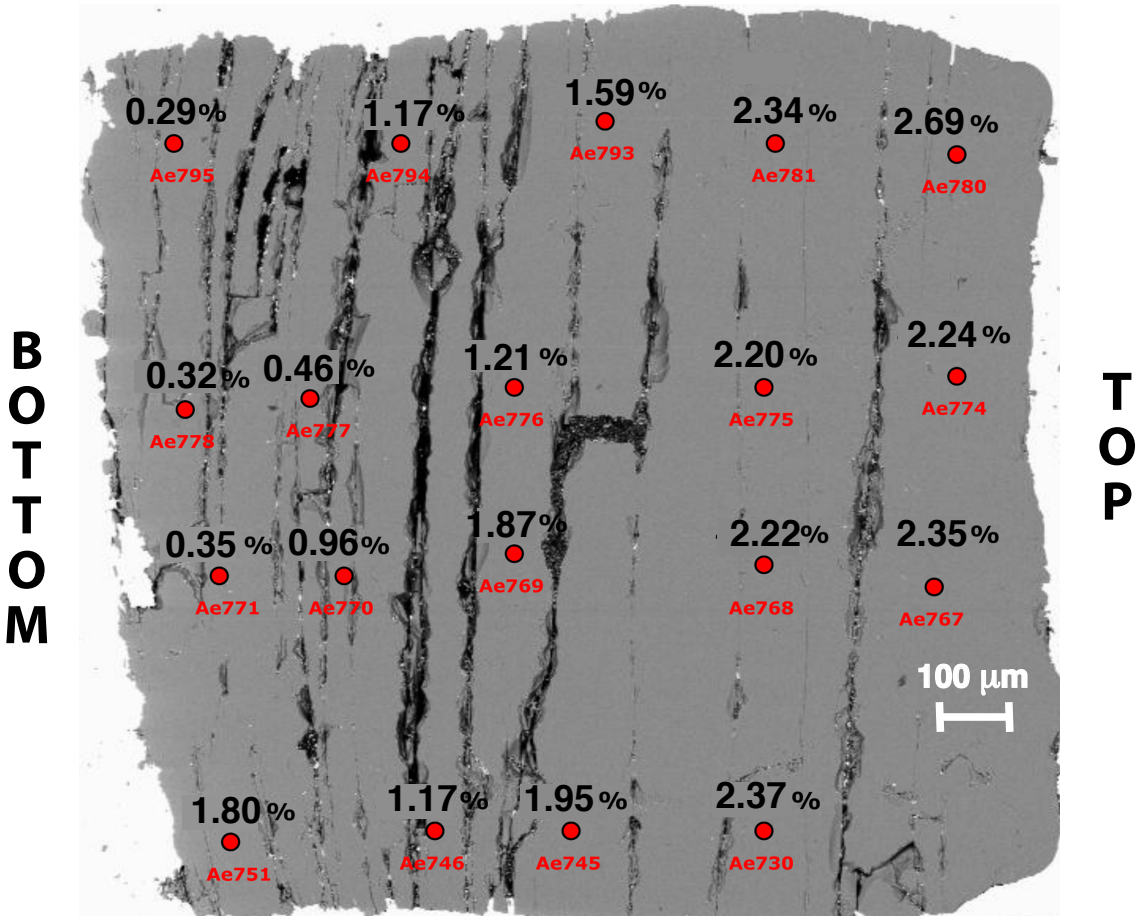

1647
1648
1649 Figure 4a
1650
1651
1652
1653
1654
1655
1656
1657
1658

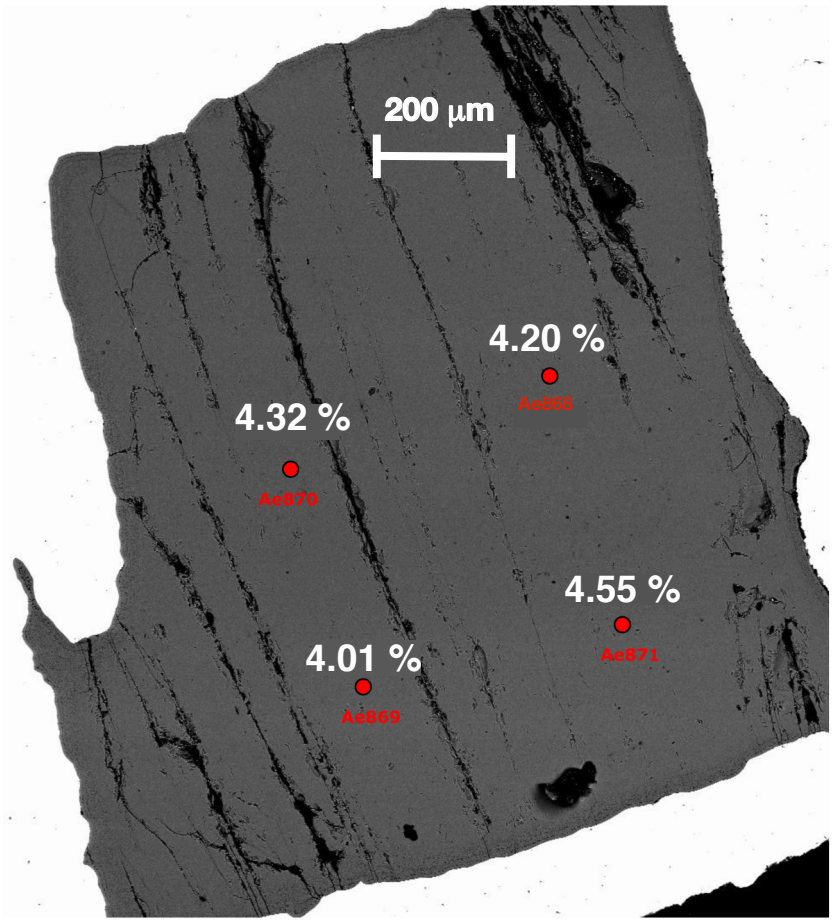

Figure 4b

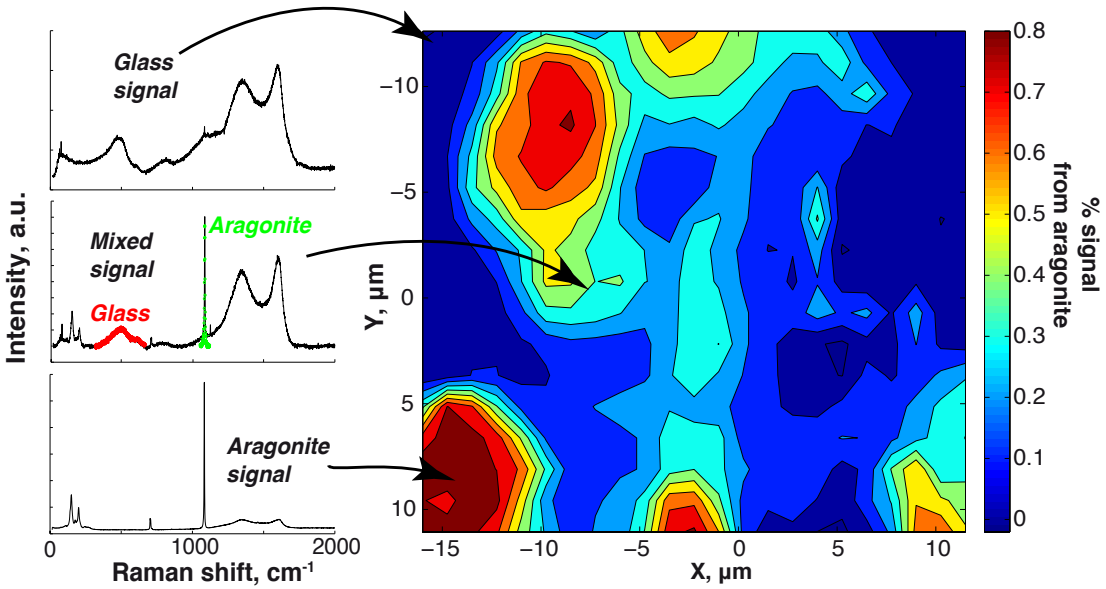
Glass
signal
Mixed
signal
Aragonite
Glass
Aragonite
signal
Intensity, a.u.
0
1000
2000
Raman shift, cm-1
−10
−5
0
5
10
Y, µm
−15
−10
−5
0
5
10
X, µm
0.8
0.7
0.6
0.5
0.4
0.3
0.2
0.1
0
% signal
from aragonite

Figure 5

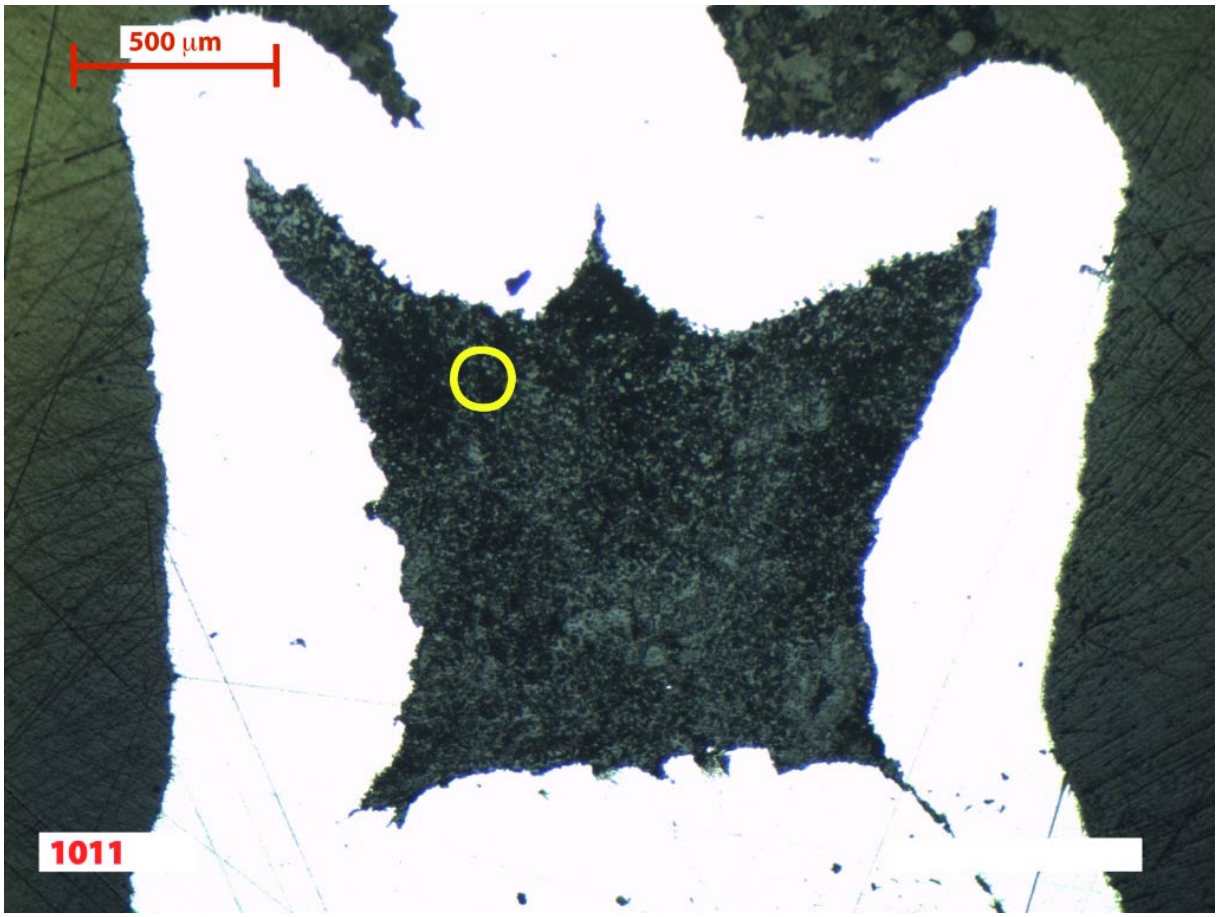

Figure 6

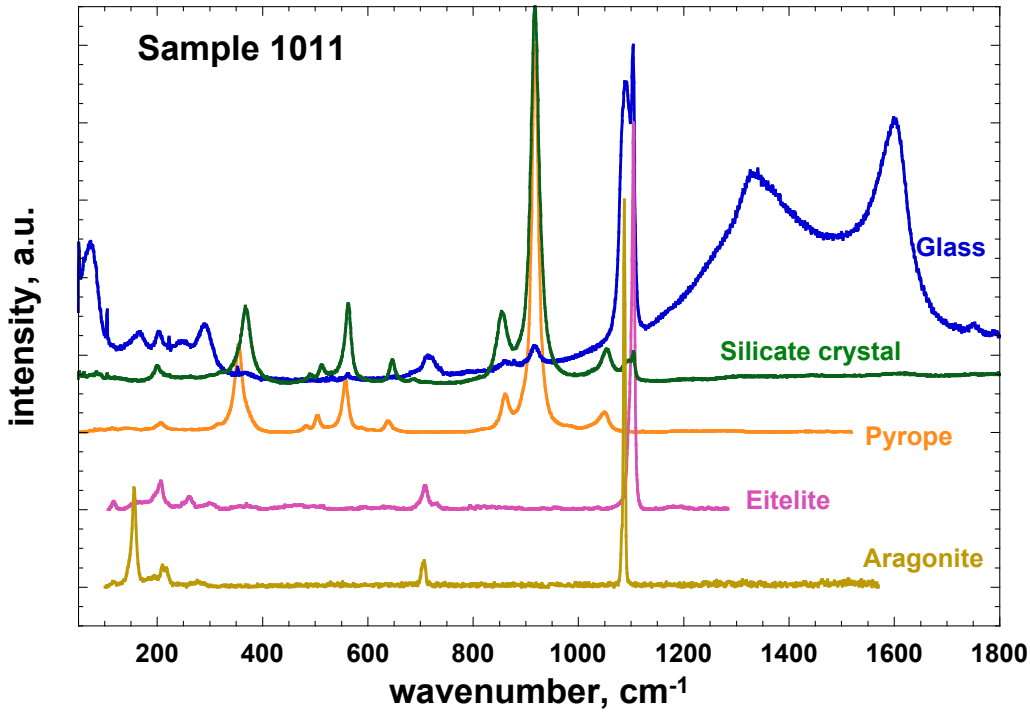
Sample 1011
intensity, a.u.
Glass
Silicate crystal
Pyrope
Eitelite
Aragonite
200
400
600
800
1000
1200
1400
1600
1800
wavenumber, cm-1

Figure 7

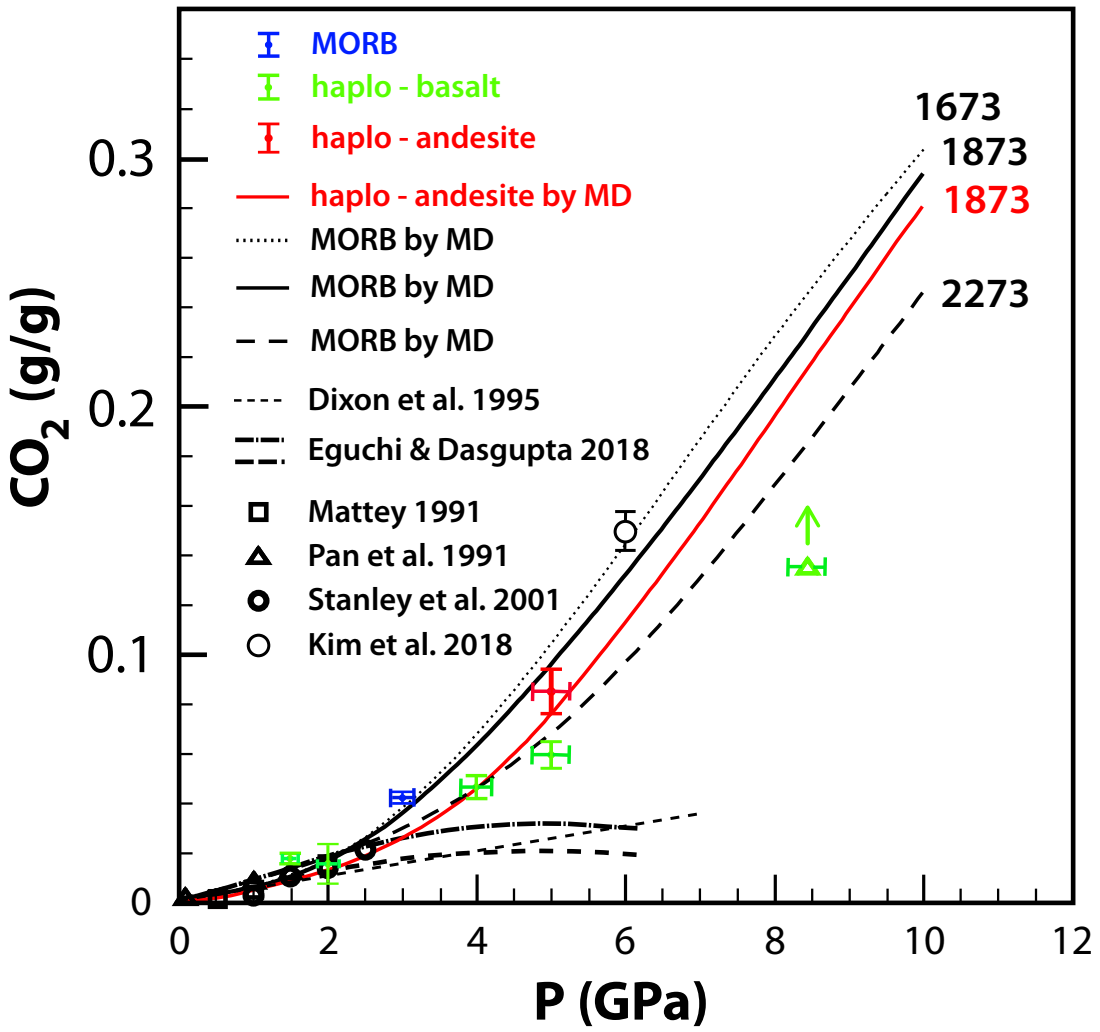
MORB
haplo - basalt
haplo - andesite
haplo - andesite by MD
MORB by MD
MORB by MD
MORB by MD
Dixon et al. 1995
Eguchi & Dasgupta 2018
Mattey 1991
Pan et al. 1991
Stanley et al. 2001
Kim et al. 2018
1673
1873
1873
2273
OH
CO_2 (g/g)
0
0.1
0.2
0.3
0
2
4
6
8
10
12
P (GPa)

Figure 8

Supplement to

Raman spectroscopy to determine CO_2 solubility in mafic silicate melts at high pressure: haplobasaltic, haploandesitic and approach to basaltic compositions

2. Experimental set up

2.1. Starting materials and high-pressure experiments

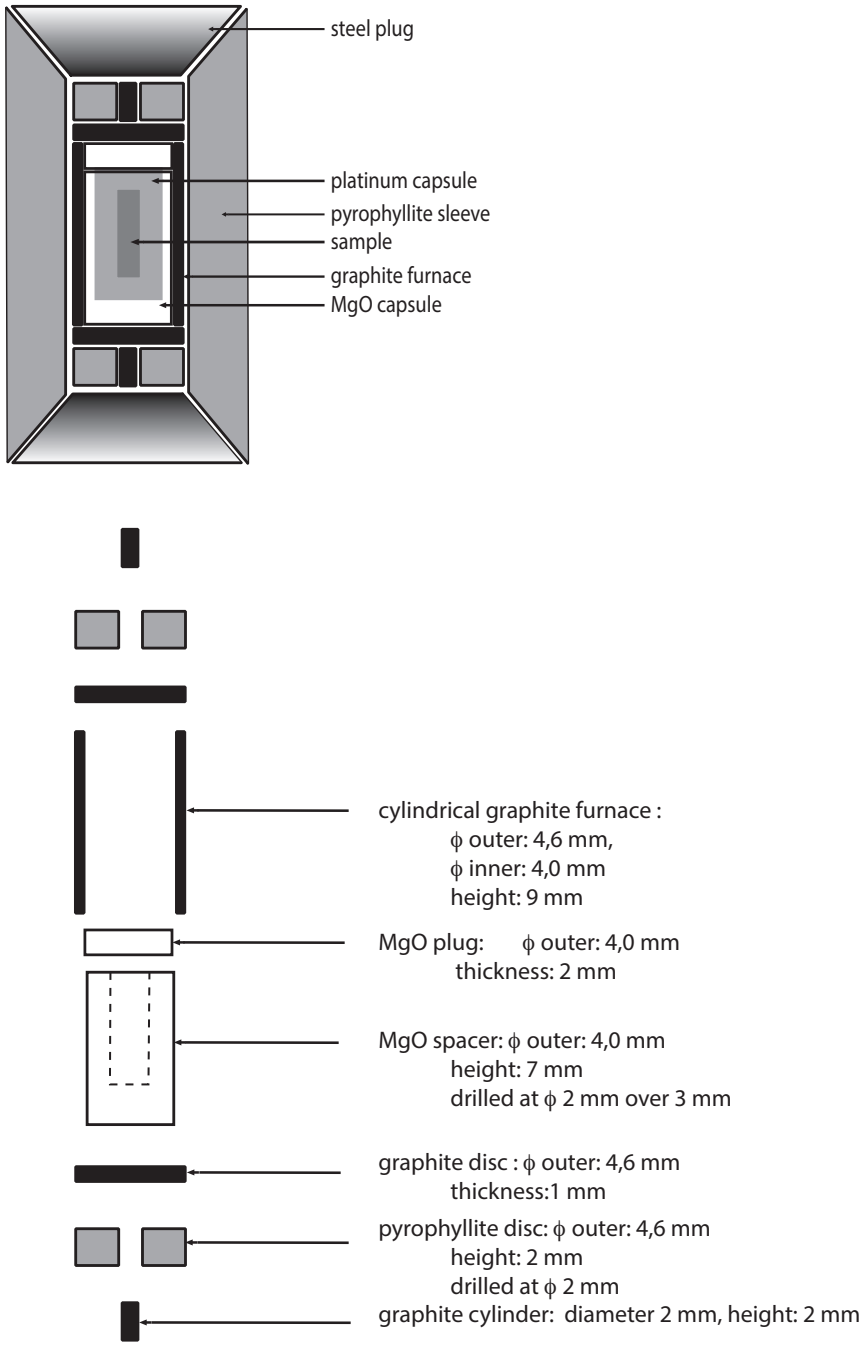

Figure S1: schematic cross section (top) and layout (bottom) of the high-pressure cell used in the Belt press for BPhE samples.

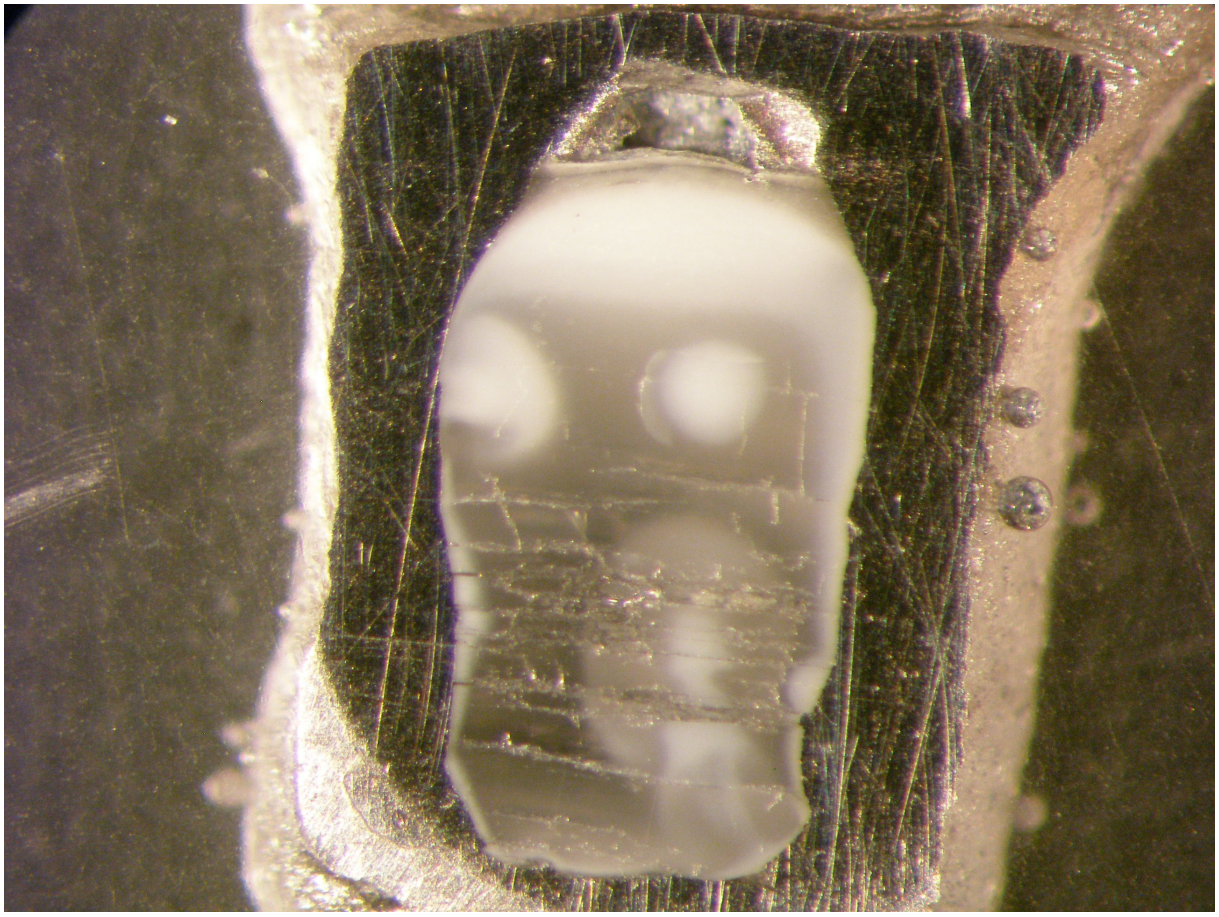

Figure S2a: Photograph of polished capsule BPhE11 (4GPa, 2130K), showing a cavity inside the platinum, at the top of the sample, opened by abrasion. This cavity must have been filled with fluid CO_2 at high P and high T.
Analysis with SEM shows that the texture is that of a glass, bearing abundant and very small crystallites (micron size), which generate the visible whitish regions sometimes with globule forms. These crystallites are not carbonate, but silicate crystals. The height of the capsule is roughly 1.5 mm.

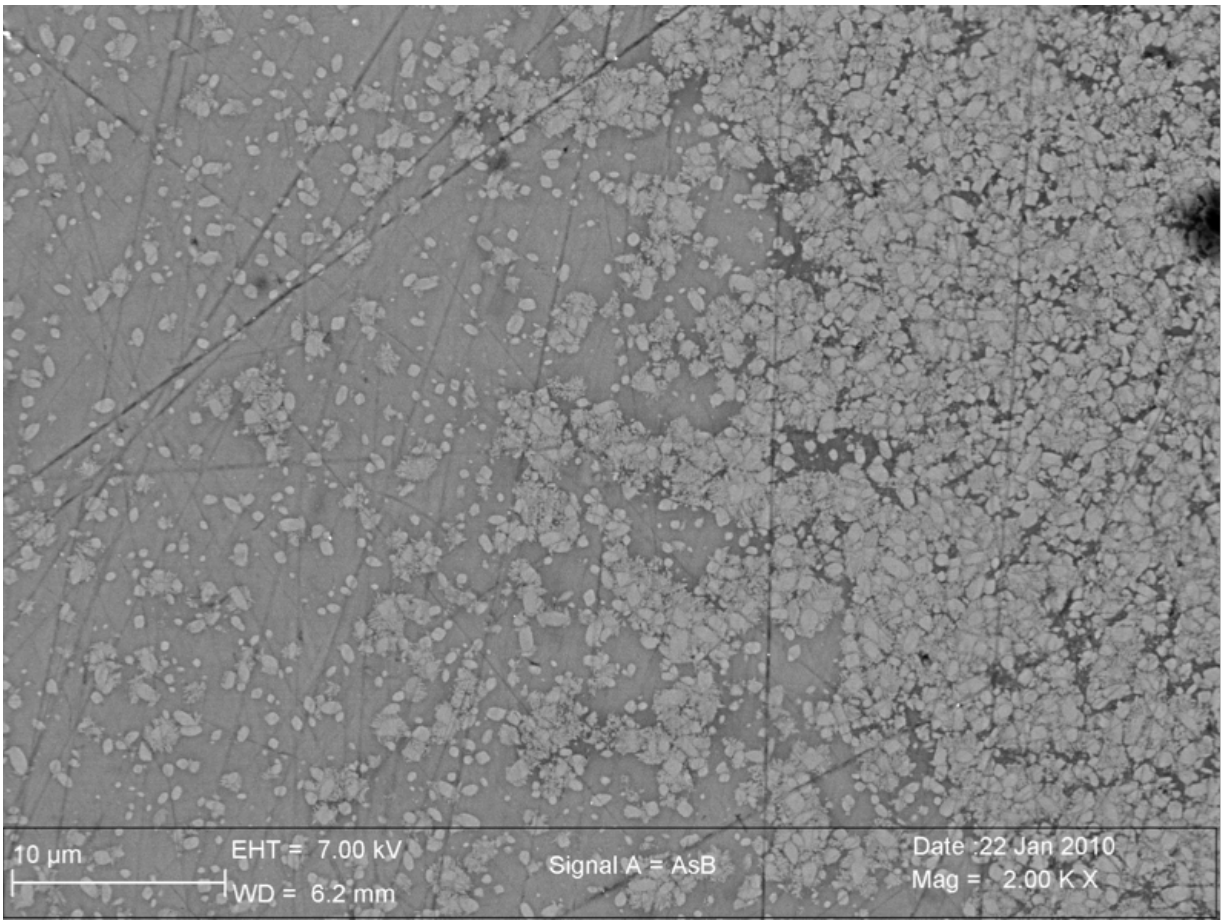

Figure S2b: MEB image of sample BPhE11 at the limit of a globule (the globule is on the right side). The structure is that of a glass with micron-sized crystallites. The globule is only a region with more crystallites. Magnification is 2000.

2.2. Raman spectroscopy analyzes

Raman spectrometry

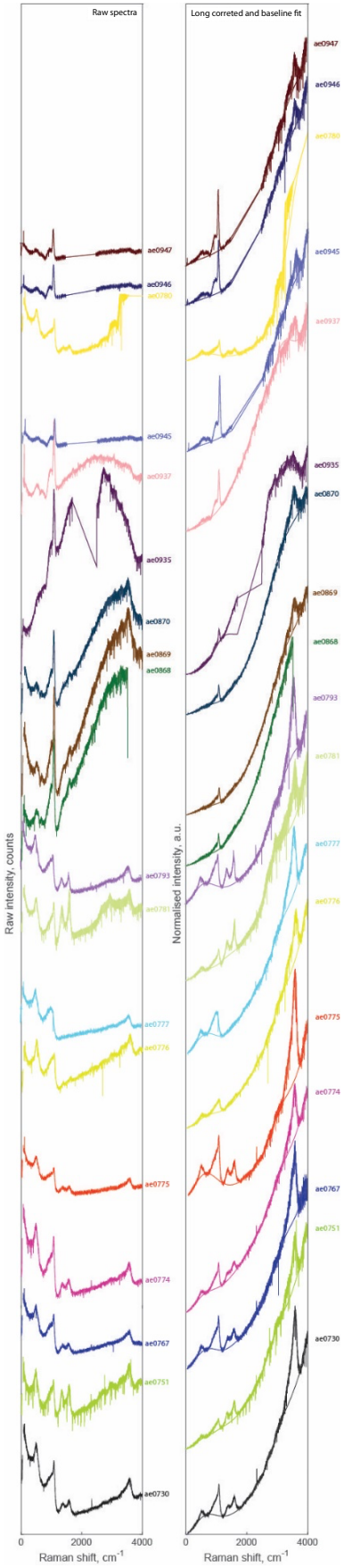

Figure S3: raw Raman spectra and spectra after the Long correction and baseline fit.

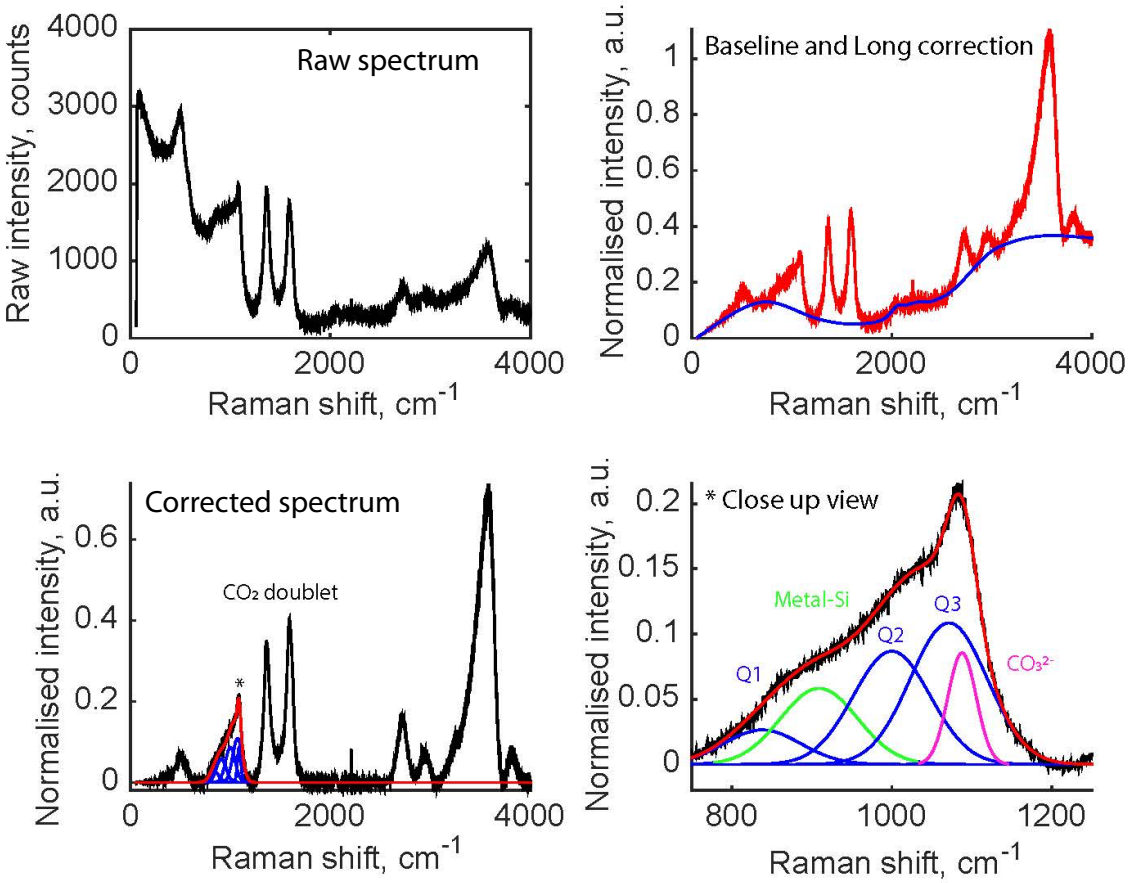

Figure S4: illustration of the four main stages of a typical spectrum treatment. Shown are the raw data (top left), on which the Long correction and baseline determination are applied (top right). The spectrum resulting from baseline subtraction is shown on the bottom left corner. Finally, a close-up view on the 800 – 1200 cm^{-1} Raman wavenumber range (star) is displayed on the bottom right showing the Q^n species, the metal-Si stretching mode and the CO_3^{2-} peak representing the CO_2 concentration in the sample.

2.3. CO_2-related Raman peaks and calibration

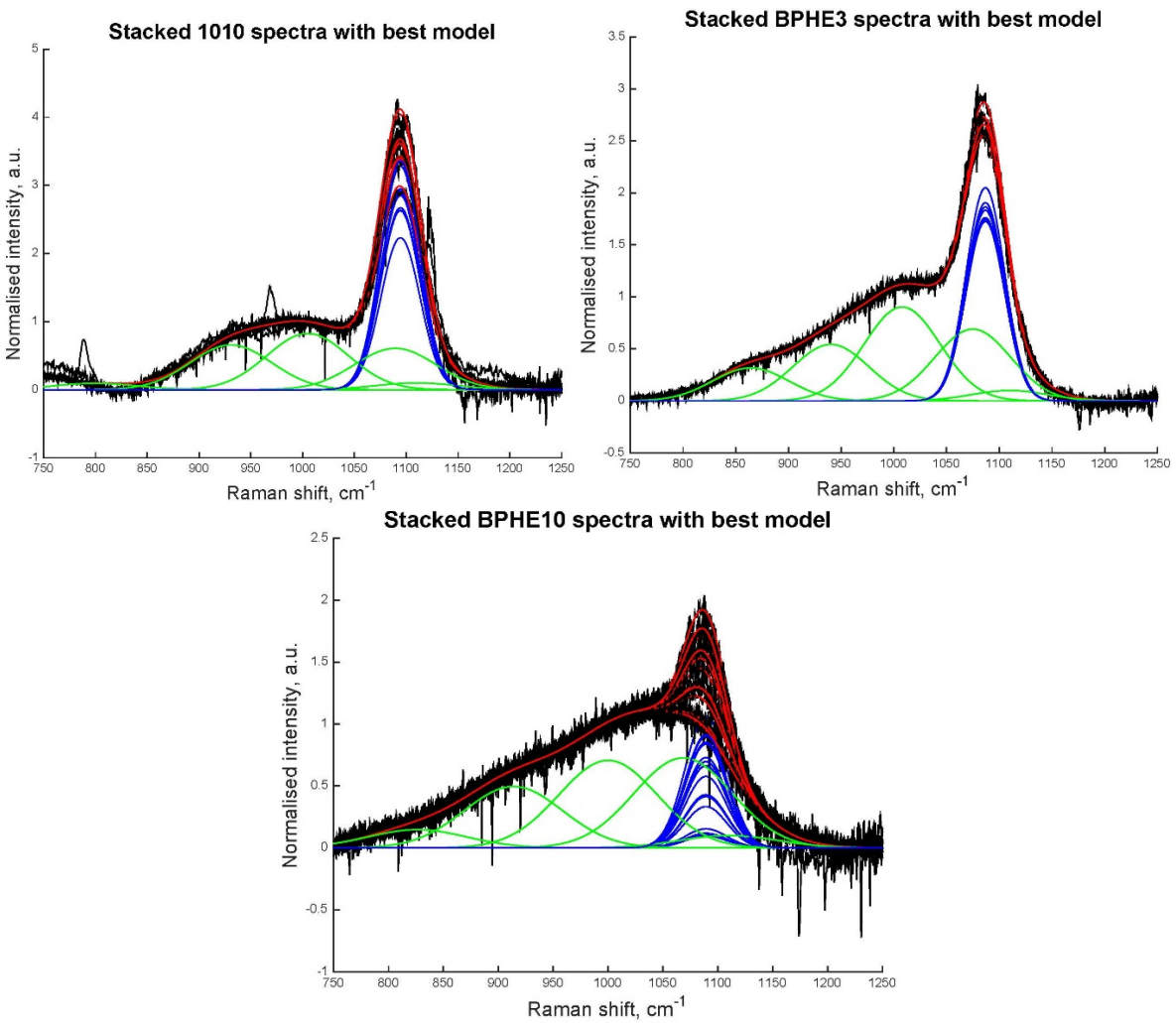

Figure S5: Close up look at the 800-1250 cm^{-1} Raman wavenumber range for samples 1010, BPHE3 and BPHE10. All the spectra and their deconvolution are stacked for each sample. The green peaks represent the Q^n species and the stacked blue peaks the CO_3^{2-}, for which different peak heights are related to different CO_3^{2-} concentrations at various places in the samples.

Sample BPhE3 (3 Gpa, 2003 K)			Sample BPhE10 (2 Gpa, 1920 K)			Sample 1010 (5 Gpa, 1873 K)		
Spectrum label	H_2O (wt.%)	CO_2 relative area (a.u.)	Spectrum label	H_2O (wt.%)	CO_2 relative area (a.u.)	Spectrum label	H_2O (wt.%)	CO_2 relative area (a.u.)
ad4498	2.1901	0.26969	ae0795	1.3441	0.018681	ae0874	0.43054	0.35598
ad4499	2.3095	0.25679	ae0794	1.3229	0.074502	ae0948	0.50306	0.37804
ad4502	2.6353	0.2588	ae0793	1.6143	0.10062	ae0946	0.50564	0.35994
ae0871	2.065	0.28874	ae0781	3.4	0.14837	ae0933	0.86748	0.40856
ae0869	2.9206	0.25467	ae0780	3.1284	0.17085	ae0943	0.85069	0.37496
ae0870	3.1626	0.27394	ae0778	2.7967	0.020315	ae0937	0.40289	0.35671
			ae0777	1.8005	0.029012	ae944	0.84705	0.44013
			ae0776	2.8326	0.076898	ae0947	0.53026	0.37532
			ae0775	2.0979	0.13983	ae0945	0.47636	0.38297
			ae0774	1.9007	0.14208	ae0875	0.50322	0.38063
			ae0771	1.6017	0.022478	ae0936	0.54746	0.31947
			ae0770	1.9941	0.060812	ae0935	0.35416	0.41422
			ae0769	2.3624	0.11894			
			ae0768	1.7992	0.1408			
			ae0767	1.8418	0.14943			
			ae0751	3.4366	0.11393			
			ae0746	3.6465	0.074404			
			ae0745	1.5936	0.12386			
			ae0730	2.2122	0.15033			

Table S1: H_2O (wt.%) results and CO_2 normalized area (arbitrary units) for each Raman spot on 3 samples.

3.3. Partially crystallized sample 1090 (5 GPa)

Mean CO_2 content from optical estimate of phenocryst proportion

After subtracting the black glitches due to sample polishing (Fig. S6), we converted the grey-scale picture in a black and white picture, with a threshold chosen to discriminate glass from crystals. We obtained the area fraction of aragonite phenocrysts that we assume to be close to the volume fraction, V_c.

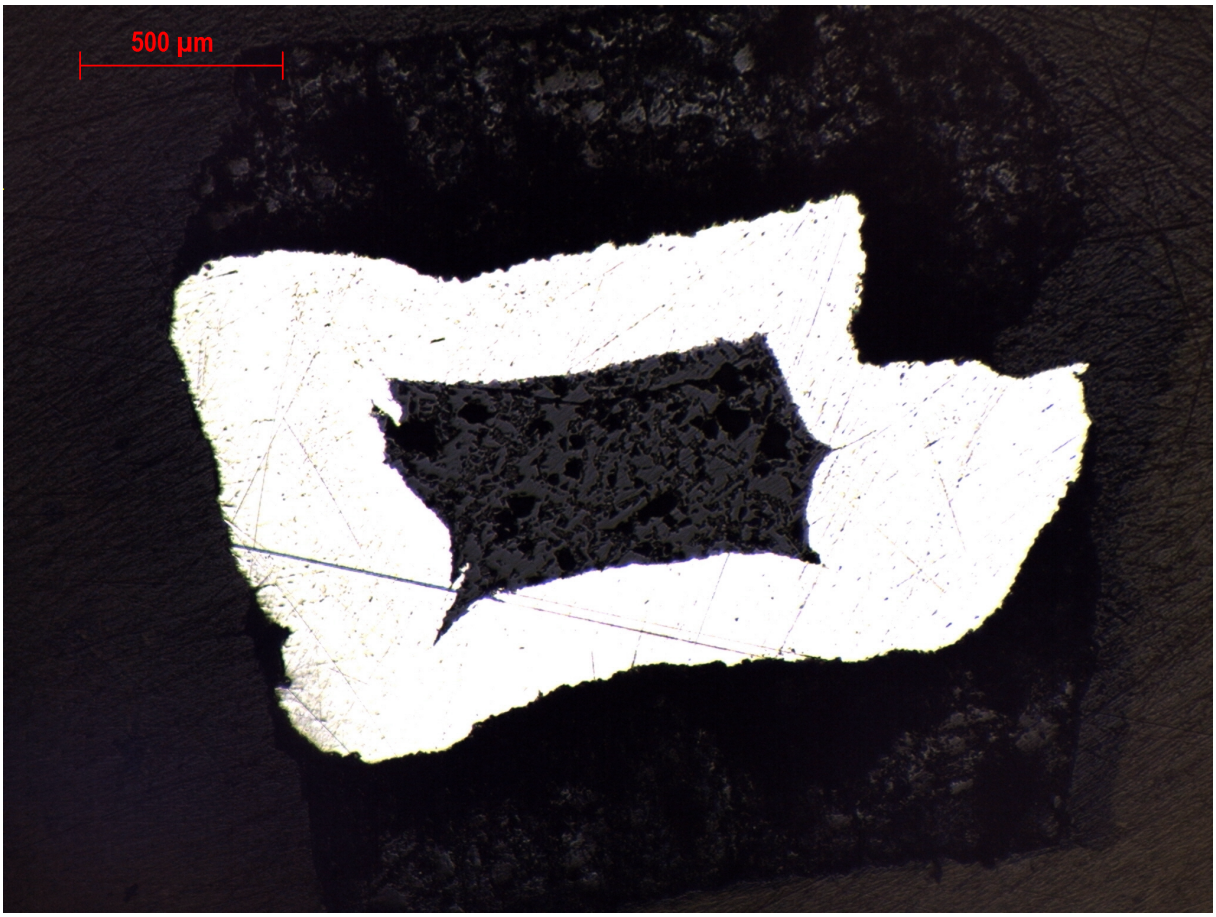

Figure S6a: Picture of sample 1090 in reflected light. No nubble is seen.

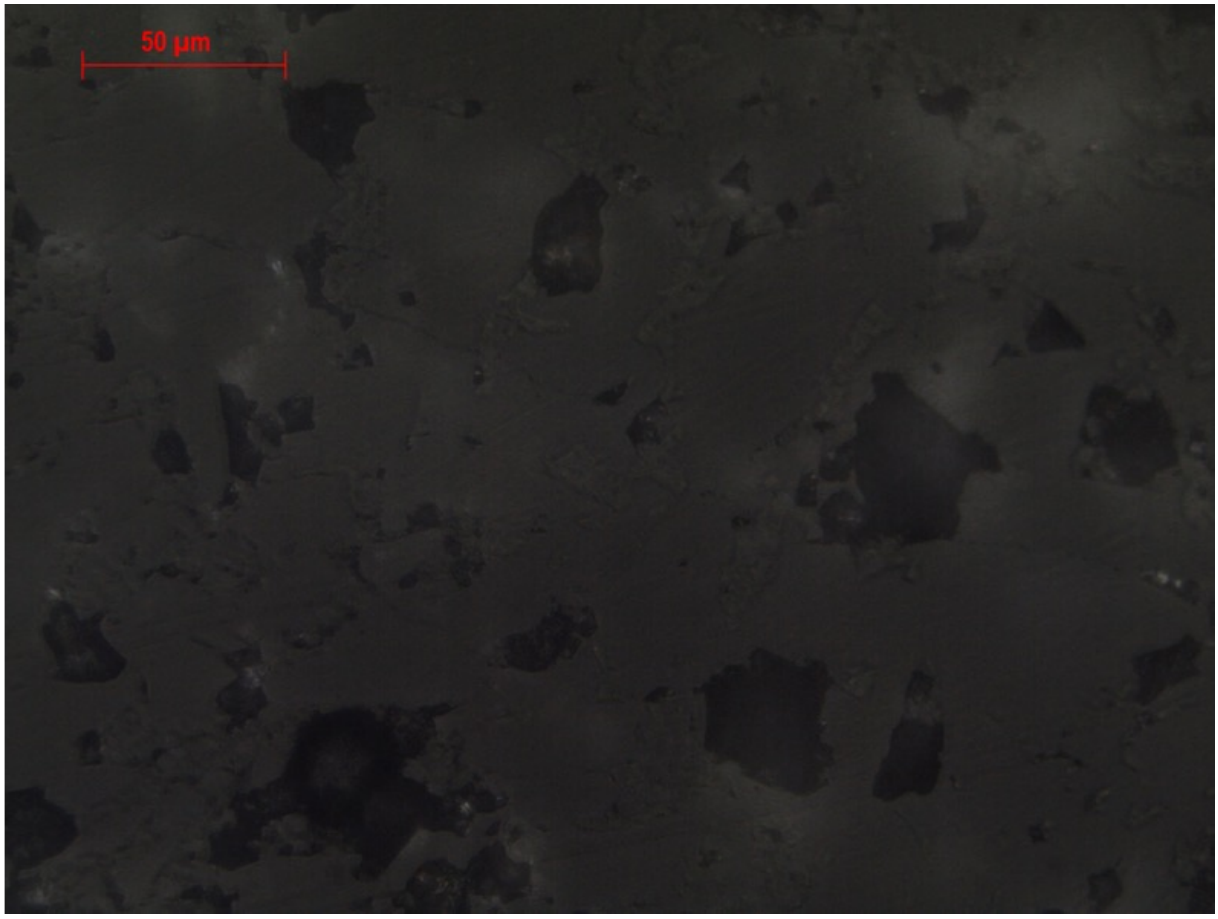

Figure S6b: Close-up of sample 1090 in reflected light. The black zones are glitches due poor polishing. One can see glass and crystals intermingled. Crystals appear slightly clearer than glass.

The corresponding CO_2 content can then be deduced by the following relationship,

$$C_{CO_2}(wt.\%) = 100 \times \frac{n_{CaCO_3} \times \left(\frac{M_{CO_2}}{M_{CaCO_3}}\right)}{n_{CaCO_3} + n_{glass} \times \left(\frac{1-V_c}{V_c}\right)} \quad \text{(S3)}$$

where n_{CaCO_3} is the density of aragonite, M_{CO_2} the molar mass of CO_2, M_{CaCO_3} the molar mass of $CaCO_3$, n_{glass} the density of the glass.

At atmospheric pressure, the density of aragonite is 2.93 g/cm3 at 300 K, and that of glass, assuming the chemical composition listed in Table 2, is ~2.49 g/cm3 at 300 K using Lange and Carmichael (1987). We found *Vc* = 18±2 vol% yielding a CO_2 content of 9±1 wt.%.

Micrometric scale Raman mapping of groundmass

We measured the area, named A_{1085}, of the CO_3^{2-} sharp peak seen in glass (the carbonate vibration in aragonite at 1085 cm^{-1}), and the area, named $A_{1085}^{aragonite}$, of the same peak in a large aragonite crystal chosen in the sample (Fig. 5). Because the intensity of a vibration band is proportional to the concentration of vibrators per unit volume, the ratio $R_{1085} = A_{1085}/A_{1085}^{aragonite}$ is then related to the CO_2 concentration borne by crystallites by the following relation

$$C_{CO_2}(wt.\%) = 100 \times R_{1085} \times \left(\frac{M_{CO_2}}{M_{melt}}\right) \quad \text{(S4)}$$

where M_{CO_2} is the molar mass of CO_2 and M_{melt} that of the melt. This is because the intensity of a vibration band is proportional to the concentration of vibrators per unit volume seen by the laser beam.

Our evaluation gives R_{1085} = 0.1137 by averaging over a 30 micrometers X 30 micrometers region. To calculate the molar mass of melt, we should use the starting chemical composition of this sample including the initial CO_2 charge of 9.0 wt.% (Table 1): we find a value of 62.04 g/mol (64.66 g/mol for the pure silicate). Using the latter value, the derived CO_2 abundance amounts to 8.1 wt.%, this value representing the carbonate microcrystals in the groundmass.

4. Discussion

4.1. CO_2 solubility in basaltic and andesitic melts up to 8.5 GPa

Comparison to previous data and accuracy of results

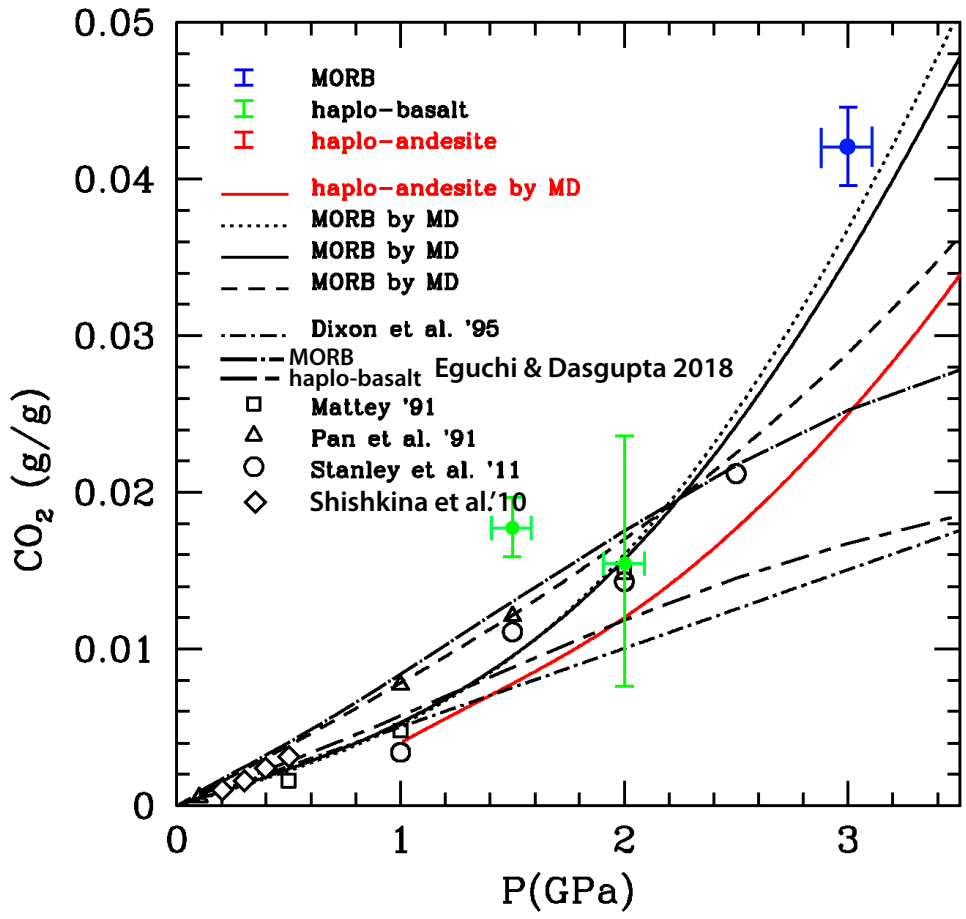

Figure S7:

Zoom on the low-pressure side of Fig. 8, showing measured values for mafic compositions, and our simulation curves, as well as other data from Pan et al. (1991), Mattey (1991), Stanley et al. (2011) and Shishkina et al. (2010; except two points < 0.2 GPa). Some data between 0 and <0.2 GPa are impossible to show here (e.g., Stolper and Holloway (1988), Pawley et al. (1992), Dixon et al. (1995), Jendrzejewski et al. (1997), Botcharnikov et al. (2005). Are also shown the straight line corresponding to the Henry's law of Dixon et al. (1995) and the recent thermodynamic model of Eguchi and Dasguspta (2018) for MORB (higher curve) and haplo-basaltic compositions (lower curve).

4.3. Influence of melt composition

Relation to melt properties and solvation structure.

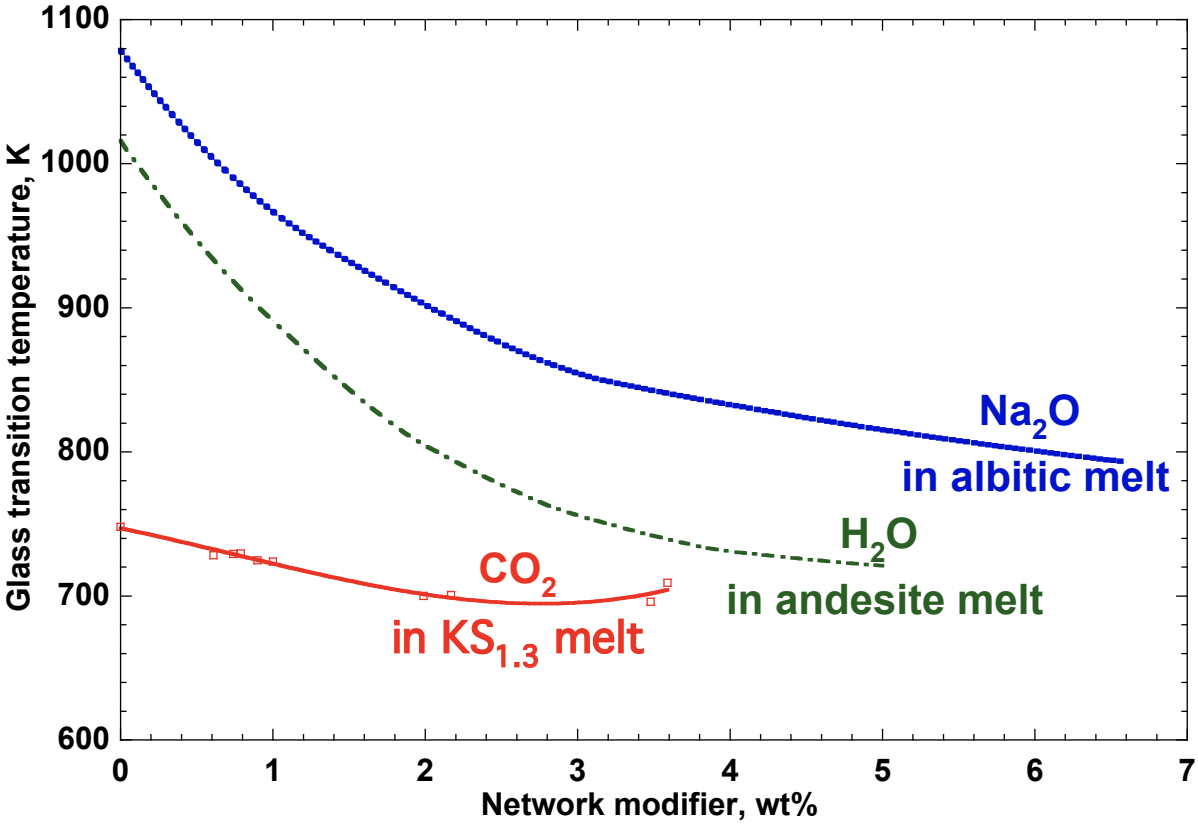

Figure S8: Influence of CO_2 dissolution on the glass transition temperature of K_2OSiO_2 melt, compared to dissolution of H_2O in andesite melt and of Na_2O in albitic melt. Data from Bourgue and Richet (2001) for CO_2 in KS; Vetere et al. (2006) for H_2O in andesite; Le Losq et al. (2014) for Na_2O in albite melt.

1939